

Article

Patterning Behavior of Hybrid Buoyancy-Marangoni Convection in Inclined Layers Heated from Below

Wasim Waris and Marcello Lappa * 

Department of Mechanical and Aerospace Engineering, University of Strathclyde, James Weir Building, 75 Montrose Street, Glasgow G1 1XJ, UK

* Correspondence: marcello.lappa@strath.ac.uk

Abstract: Alongside classical effects driven by gravity or surface tension in non-isothermal fluids, the present experimental study concentrates on other exotic (poorly known) modes of convection, which are enabled in a fluid layer delimited from below by a hot plate and unbounded from above when its container is inclined to the horizontal direction. By means of a concerted approach based on the application of a thermographic visualization technique, multiple temperature measurements at different points and a posteriori computer-based reconstruction of the spatial distribution of wavelengths, it is shown that this fluid-dynamic system is prone to develop a rich set of patterns. These include (but are not limited to), spatially localized (compact) cells, longitudinal wavy rolls, various defects produced by other instabilities and finger-like structures resulting from an interesting roll pinching mechanism (by which a single longitudinal roll can be split into two neighboring rolls with smaller wavelength). Through parametric variation of the tilt angle, the imposed temperature difference and the volume of liquid employed, it is inferred that the observable dynamics are driven by the ability of gravity-induced shear flow to break the in-plane isotropy of the system, the relative importance of surface-tension-driven and buoyancy effects, and the spatially varying depth of the layer. Some effort is provided to identify universality classes and similarities with other out-of-equilibrium thermal systems, which have attracted significant attention in the literature.

Keywords: Marangoni convection; hydrothermal wave; solid particles; patterning behavior



Citation: Waris, W.; Lappa, M.

Patterning Behavior of Hybrid Buoyancy-Marangoni Convection in Inclined Layers Heated from Below. *Fluids* **2023**, *8*, 12. <https://doi.org/10.3390/fluids8010012>

Academic Editor: Mehrdad Massoudi

Received: 23 November 2022

Revised: 24 December 2022

Accepted: 28 December 2022

Published: 29 December 2022



Copyright: © 2022 by the authors. Licensee MDPI, Basel, Switzerland. This article is an open access article distributed under the terms and conditions of the Creative Commons Attribution (CC BY) license (<https://creativecommons.org/licenses/by/4.0/>).

1. Introduction

In this study, the properties of mixed buoyancy-Marangoni convection are investigated in an inclined layer uniformly heated from below and unbounded from above (in contact with a gaseous ambient at constant temperature). A justification for our interest in this specific subject stems from the paucity of similar results in the literature. Apart from the relevance of this problem to the general kingdom of thermal convection (which naturally makes it a fundamental topic of interest to fluid physicists and other scholars), additional obvious aspects making it a subject worthy of analysis are the various areas of applications it is somehow connected to. A first example is represented by the sector of crystal ‘growth from the melt’, where crystals of materials of various kinds (e.g., silicon, semiconductors or oxides) to be used for advanced electronic or opto-electronic devices are typically produced through melting and re-solidification ‘in well-controlled conditions’ of an initially polycrystalline substance; it is known that even tilt angles as small as 0.5° can cause non-axisymmetric growth conditions in such processes and related detrimental effects (see, e.g., Markham and Rosenberger [1]; Bachran et al. [2]; Mizev and Schwabe [3]).

Similar concepts apply to the solidification of metal alloys (e.g., Jones [4]; Coriell et al. [5]; Webb and Viskanta [6]; Forth and Wheeler [7]) where inclination-induced shear flow can lead to serious morphological instabilities. Another relevant case is represented by phase change materials (PCMs), typically used in ‘energy-saving’ applications. These substances (ideally suited to store energy during melting and release it during solidification) can

support during these repeated cycles of solid/liquid transition the emergence of both buoyancy and surface-tension driven convection (Lappa [8]); moreover, the liquid domain produced accordingly has often a variable depth (see, e.g., Salgado Sanchez et al. [9,10]).

In all these instances, mixed buoyancy-Marangoni convection can be produced by gradients of temperature (Lappa [11]), gradients of concentration (Zhang et al. [12]) or both effects (Boura and Gebhart [13], Qin and Grigoriev [14]). In the present study, we concentrate on the situation where convection is produced by thermal effects only. In particular, the reader is referred to Figure 1 for the required details about the configuration used here to ‘mimic’ situations such as those occurring in the abovementioned technological applications. The greater proximity of the free surface to the heated bottom in the areas where the depth of the layer is smaller is responsible for the emergence of a temperature inhomogeneity at the interface, thereby giving rise to fluid convection directly driven by the Marangoni effect. This flow is also supported by buoyancy. Indeed, the component of gravity parallel to the bottom plate, causes relatively warm fluid to flow up along this wall (from left to right in Figure 1) and in the opposite direction along the free interface. The magnitude ratio of buoyant and surface-tension-driven effects can be varied by changing the overall amount of fluid, i.e., its average depth. The larger the depth, the higher the relative importance of gravitational effects in comparison to surface tension ones. The most important implication of this observation is that relevant links also exist between this problem and a series of problems of meteorological, oceanographic and geophysical interest (see, e.g., Lipps [15] and Thorpe [16] for the atmosphere; Farrow and Patterson [17] for the hydrosphere and Richter [18] for analogous considerations about the mantle of our planet).

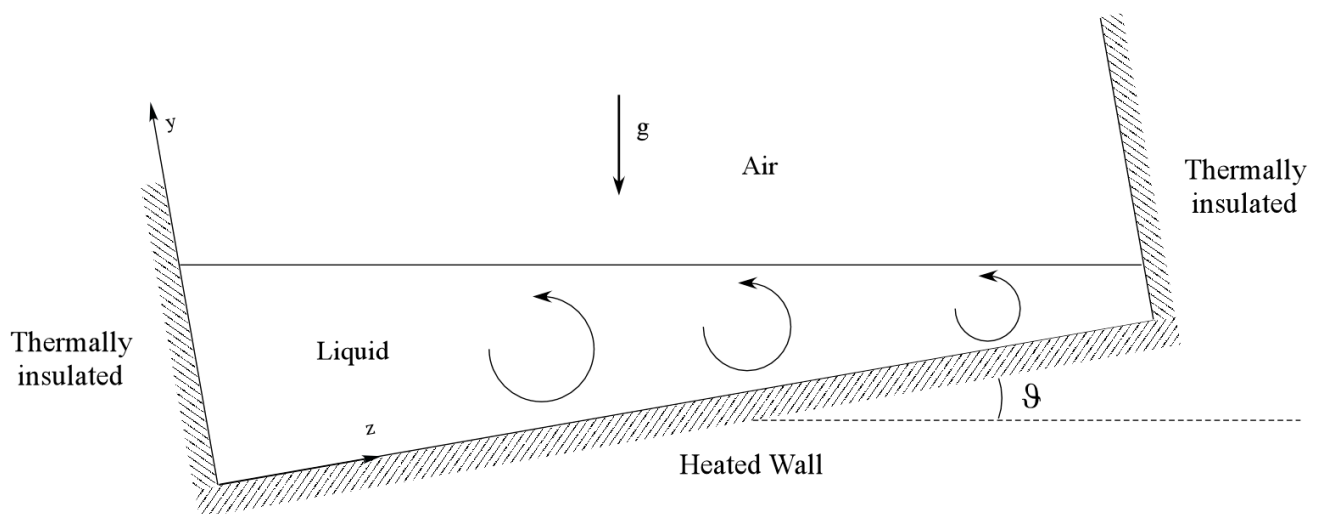


Figure 1. Sketch of the considered problem.

It is also worth noting that, from a purely theoretical standpoint, the considered problem may be regarded as a specific realization of a more general category of phenomena where a ‘shear flow’ breaks the in-plane isotropy of the system (see, e.g., Weber [19]). This effect can cause a deviation from the known dynamics of out-of-equilibrium systems, which are invariant with respect to translations in a direction parallel to the bottom boundary such as the canonical Rayleigh-Bénard and Marangoni-Bénard flows.

Until now, the former has been explored for fluid domains with “uniform thickness” tilted with respect to the horizontal direction. In these cases, the isotropy is lost due to the mismatch in the symmetry of the boundary conditions in relation to the applied body force (gravity). This condition can make the perfect stationary bifurcation typical of Rayleigh-Bénard (RB) convection structurally “unstable to the tilt” (and “imperfect” even if the tilt angle is as small as $O(10^{-3})$, see Cliffe and Winters [20]; Mizushima and Adachi [21]). Studies conducted in the past two decades have conclusively established that, depending

on the inclination, the considered fluid, the size of the system and the applied temperature difference, many complexities and a rich variety of flow phenomena can take place. Works of relevance to the subject include those by Clever and Busse [22], Weber [23], Chen and Pearlstein [24], Shadid and Goldstein [25], Busse and Clever [26], Fujimura and Kelly [27], Kaloni and Qiao [28].

According to all these studies, the emerging (gravitational) modes of convection in tilted enclosures can be broadly classified/categorized into two groups; namely, transverse rolls and longitudinal rolls. A dichotomy is generally introduced between these because, while the former have essentially a shear driven nature, the latter have a strong thermal (buoyant) origin (Daniels et al. [29,30]; Tao and Busse [31]; Subramanian et al. [32]).

As even a cursory perusal of the existing literature on these subjects would immediately reveal, in comparison to gravitational convection, studies on systems driven by surface-tension-driven effects where the isotropy of the classical heated-from-below configuration is broken, are much more rare and sparse. Some interesting efforts exist for the case where the isotropy-breaking shear flow has been obtained by inclining the temperature gradient with respect to the liquid-gas interface rather than by inclining the layer itself (i.e., a temperature difference resulting from the combination of heating from below and horizontal differential heating). As an example, after the problem's initial popularization by Nepomnyashchy et al. [33] and Ueno et al. [34], additional insights into this specific situation have been provided by Shklyaev and Nepomnyashchy [35], Mizev and Schwabe [3] and Patne et al. [36]. Most interestingly, these efforts have revealed that, despite the shift in the driving force from buoyancy to Marangoni effects, the duality in terms of transverse and longitudinal modes of convection still holds in these case (with the classical compact hexagonal cells typical of Marangoni-Bénard (MB) convection being recovered only in the limit as the horizontal contribution to the overall temperature difference tends to zero).

One may therefore conclude that a line of inquiry dedicated to thermal flows and related instabilities in inclined systems (or systems with an inclined temperature gradient) only exists for the case in which the geometry has a constant thickness along the entire extension of the heated wall, which may be regarded as the main justification or motivation for the present work.

Here, the problem is tackled experimentally (see Section 2) and analyzed from both the traditional coarse-grained macroscopic (i.e., patterning behavior) perspective (see Section 3) and from a fine-grained micromechanical level in which an interpretation for the underlying mechanisms is sought in the light of the existing literature for problems that share a significant degree of similarity (see Section 4).

2. The System

2.1. The Geometry

A sketch of the considered fluid-dynamic system is shown in Figure 1. While the bottom of the cavity has a constant temperature higher than that of the external gaseous environment (air), the lateral walls are thermally insulated.

The inclination of the container causes the liquid to redistribute its volume in such a way that its surface remains perfectly horizontal with respect to an external observer (on tilting the system, the liquid-gas interface adjusts its orientation in order to remain perpendicular to gravity). Since the resulting liquid depth is not independent from the z coordinate, this naturally causes a breakage in the horizontal translational invariance (isotropy) of the system. Notably, given its spatially varying depth, the problem would not be isotropic even by replacing gravity with a force perfectly perpendicular to the bottom wall. Similarly, no isotropy would be recovered by considering a quiescent state, i.e., a condition where the fluid does not move. Obviously, the loss of horizontal translational invariance is reinforced by the presence the shear flow induced by the inclination of the heated bottom wall, which contributes to this effect as it does in classical problems dealing with inclined thermal convection in constant-thickness layers. Remarkably, all these factors

are expected to expand the set of possible solutions with respect to those identified in earlier studies.

2.2. The Liquid

The physical properties of the used fluid (Emkarate RL22H oil) as a function of the temperature are summarized in Figure 2 (these figures also include the related fitting laws in the form of polynomial expressions).

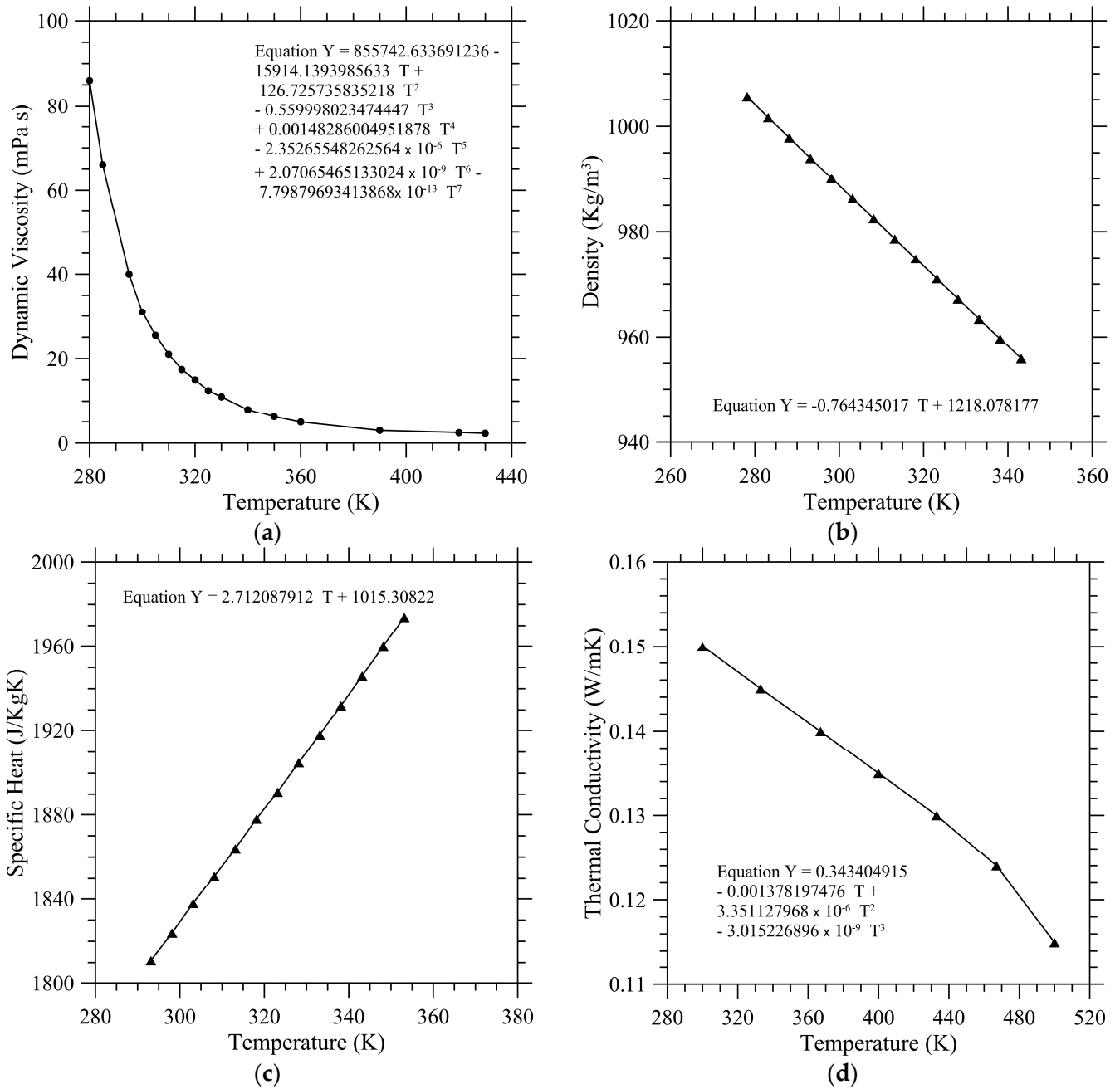


Figure 2. Cont.

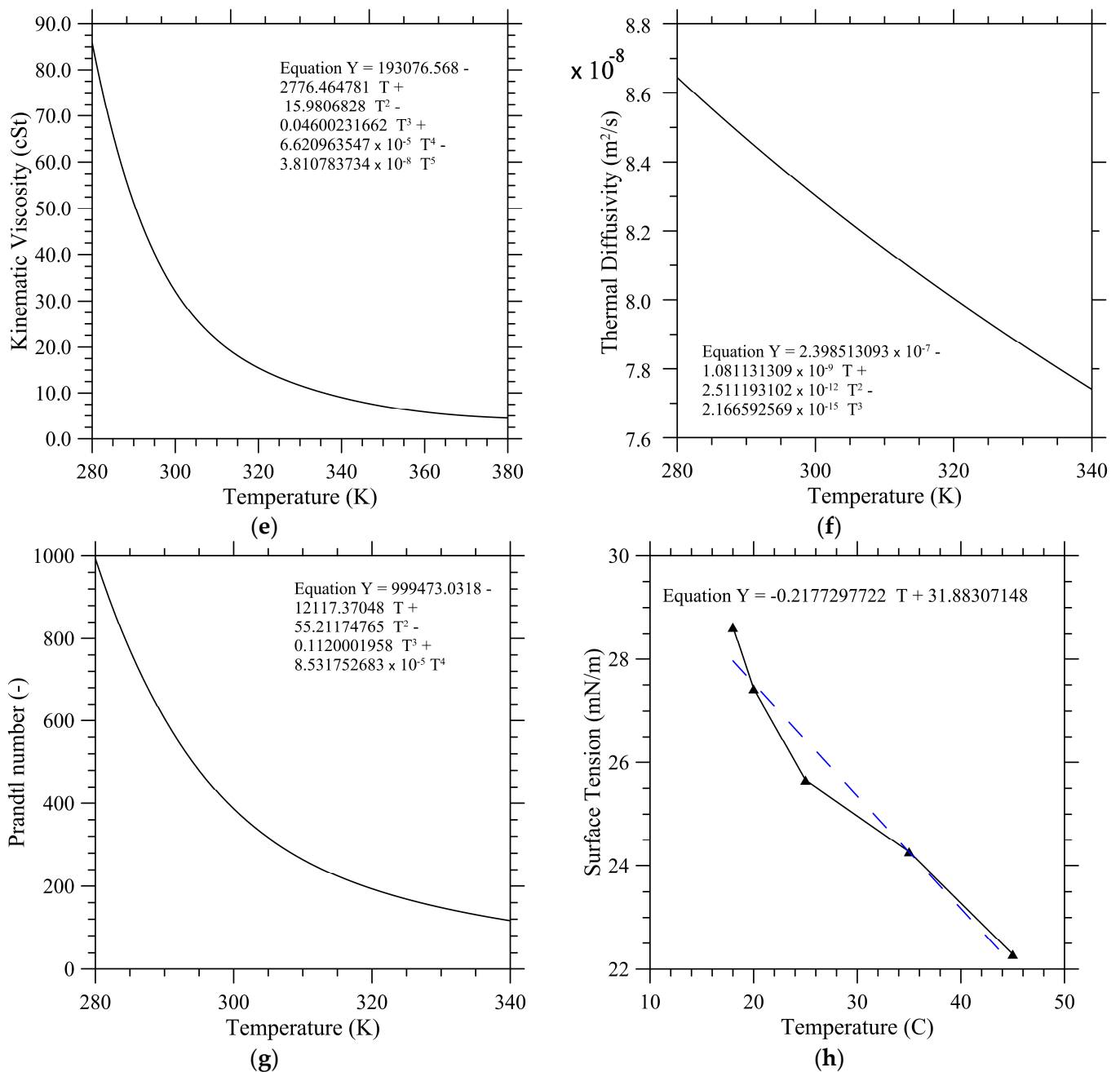


Figure 2. Physical Properties of Emkarate RL22H as a function of temperature as provided by the manufacturer: (a) Dynamic viscosity μ (exp. measurements); (b) Density ρ (exp. measurements); (c) Specific Heat at constant pressure C_p (exp. measurements); (d) Thermal conductivity λ (exp. measurements); (e) Kinematic viscosity ν (derived quantity, $\nu = \mu/\rho$, $1 \text{ cSt} = 10^{-6} \text{ m}^2/\text{s}$); (f) Thermal diffusivity α (derived quantity, $\alpha = \lambda/\rho C_p$); (g) Prandtl number (derived quantity, $Pr = \nu/\alpha$), (h) Surface tension σ .

These figures are instrumental in showing that the physical properties of the considered fluid display a variable degree of sensitivity to temperature depending on the considered property (density ρ , specific heat C_p , thermal conductivity λ , thermal diffusivity α , dynamic viscosity μ , kinematic viscosity ν). The quantities ρ , C_p , λ and α (Figures 2b, 2c, 2d and 2f, respectively) undergo a 10% percentage variation (or even smaller) over a range of 100 K. Nevertheless, the corresponding change in terms of μ and ν is much more significant (see Figures 2a and 2e, respectively).

The fluid Prandtl number can be introduced following the classical definition as:

$$\text{Pr} = \frac{\nu}{\alpha} \quad (1)$$

The dependence of this parameter on temperature can be gathered from Figure 2g where it is shown that for the considered oil a relatively high increase in the average temperature is equivalent to considering a fluid with a much smaller value of the Prandtl number (e.g., a value of the Prandtl $\text{Pr} \cong 520$ for $T \cong 20$ °C is reduced to a value as small as $\text{Pr} \cong 170$ for $T \cong 50$ °C).

2.3. Characteristic Numbers

In order to make the outcomes of the present experimental study more general, following a common practice in the literature, it is convenient to define non-dimensional groups by which the number of influential parameters can be drastically reduced and the related interpretation of the system dynamics strongly simplified. In the considered problem, these are the classical Prandtl number (Equation (1)) and the canonical Rayleigh and Marangoni numbers. Introducing the average (or “equivalent”) depth of the layer (d) as ratio between the effective volume (Ω) of liquid present in the container and the area of the container base (corresponding to constant depth of the fluid when no tilt is applied), the last two numbers can be cast in compact form as:

$$\text{Ra} = \frac{g\beta_T\Delta T d^3}{\nu_0\alpha_0} \quad (2)$$

$$\text{Ma} = \frac{\sigma_T\Delta T d}{\mu_0\alpha_0} \quad (3)$$

where ΔT accounts for a representative temperature difference, namely, the difference between the temperature of the bottom plate (T_{plate}) and that of the ambient (T_{air}), i.e., $\Delta T = T_{plate} - T_{air}$, (this temperature difference, much higher than that effective through the liquid, is used for practical purposes as the temperature of the free liquid-gas interface is not known a priori and behaves as a spatially varying quantity in the presence of convection); moreover, g and β_T are the gravity acceleration and the thermal expansion coefficient, 9.81 ms^{-2} and $\cong 7.7 \times 10^{-4} \text{ K}^{-1}$ of the considered fluid, respectively; σ_T is the surface tension derivative coefficient ($\cong 0.218 \text{ mNm}^{-1}\text{K}^{-1}$ for the considered fluid, see Figure 2h). The subscript “0” refers to a reference temperature, which in the present work, for simplicity and without loss of generality, is assumed to be the temperature T_0 of the environment (i.e., T_{air}). These two characteristic numbers can be further combined into a third non-dimensional group, generally known as the dynamic Bond number:

$$\text{Bo}_{dyn} = \frac{\text{Ra}}{\text{Ma}} = \frac{\rho g \beta_T d^2}{\sigma_T} \quad (4)$$

Although this should be regarded as a ‘derived’ parameter, the convenience in using it stems from its independence from the temperature difference and the immediate information it provides on the relative importance of buoyancy and surface-tension driven effects according to whether it is larger or smaller than 1 (buoyancy effects being more important in the former case).

3. Experimental Apparatus

The containers used for the present experiments are shown in Figure 3. They differ about both shape and size. While one container has a square symmetry and characteristic internal size 8 cm (Figure 3a), the other has the cylindrical symmetry and an internal diameter of 13.3 cm (Figure 3b). Experiments are conducted in these containers for the same conditions (same liquid depth, temperature of the bottom plate and overall system inclination) to distillate out the role played in the considered dynamics (if any) by the solid

lateral wall and the aspect ratio A of the fluid domain (defined as ratio of the container horizontal size and the depth of the liquid).

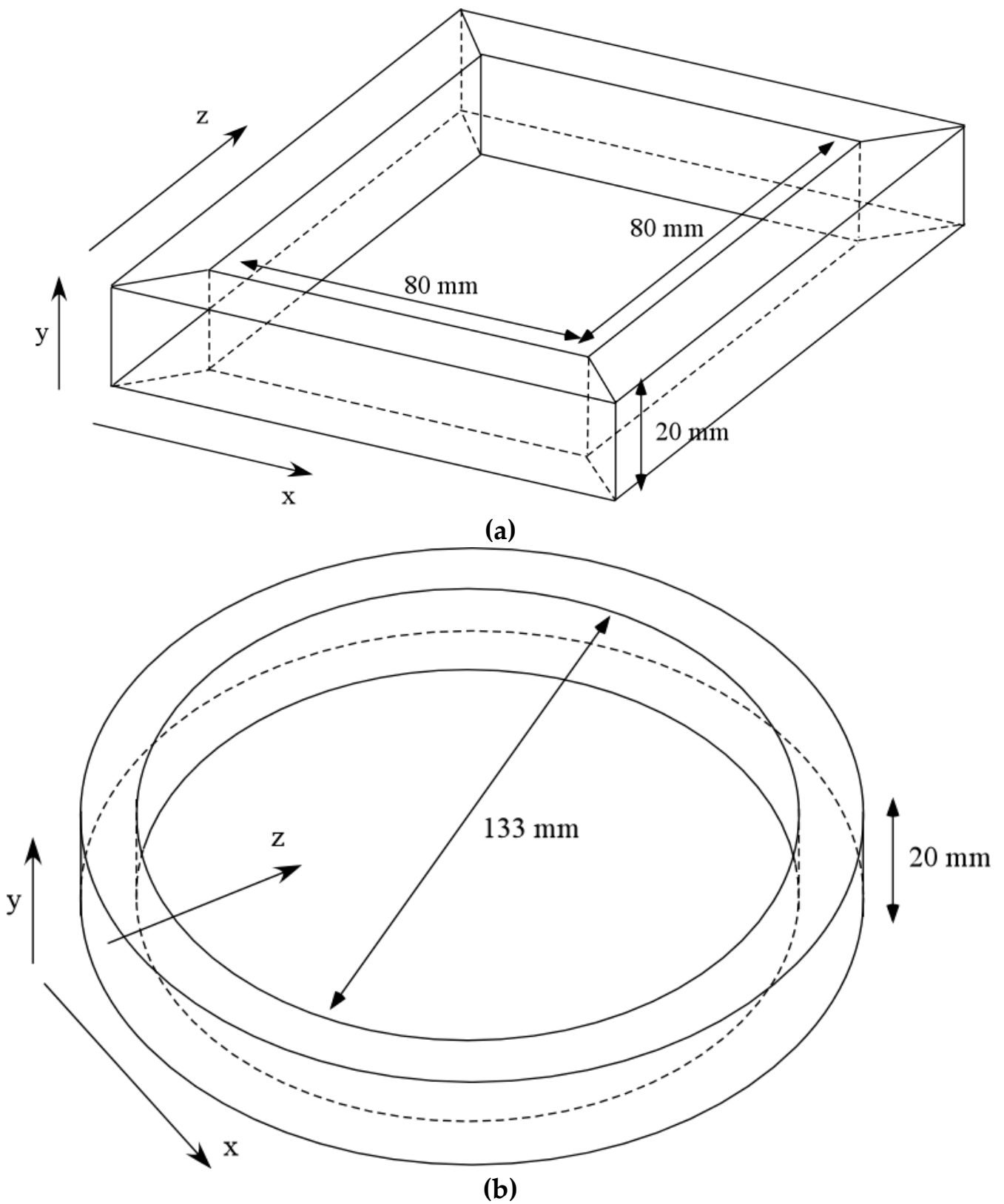


Figure 3. Three-dimensional sketch of the fluid container delimited by sidewalls of Perspex: (a) square container, (b) cylindrical container.

In order to set a well-defined temperature difference between the bottom of the container and the external environment, we rely on a commercial component, namely, a MS-H280-Pro Round ceramic coated Steel Hotplate/Stirrer, able to produce a uniform temperature T_{plate} with an accuracy of 1 °C up to 280 °C (the reader being referred to Table 1 for other specifications).

Table 1. Specifications of MS-H280-Pro Round ceramic coated Steel Hotplate/Stirrer.

Parameter	Value/Range
Work plate Dimension	Diameter 135 mm
Work plate material	Stainless steel cover with ceramic
Motor type	Brushless DC motor
Motor rating input	5 W
Motor rating output	3 W
Power	515 W
Heating output	500 W
Voltage	100–120/200–240 V 50/60 Hz
Heating temperature range	Room temp.–280, increment 1 °C
Control accuracy of work plate	±1 °C (<100 °C) ±1%(>100 °C)
External temperature sensor	PT1000 (accuracy ±0.5 °C)
Dimension [W × D × H]	150 × 260 × 80 mm
Weight	1.8 kg

In line with other successful attempts in the literature (see, e.g., Cerisier et al. [37,38]; Ismagilov et al. [39]; Chauvet et al. [40]; Wang et al. [41]; Wu et al. [42]; Sobac et al. [43]; Tönsmann et al. [44]), the distribution of temperature on the free surface of the considered liquid is observed using a FLIR C3-X Compact Thermal Imaging Camera (the related IR sensor has a resolution of 128 × 96 px and thermal sensitivity of 70 mK; moreover, it can detect and measure temperatures between −20 °C and +300 °C to an accuracy of ±3%).

The overall inclination of the system is measured using a digital inclinometer with an accuracy of 0.01° (Neoteck NTK033-V). The following cases are investigated in terms of liquid depth: $0.5 \leq d \leq 0.75$ cm corresponding to $0.86 \leq Bo_{dyn} \leq 1.94$, moreover, $T_{air} \cong 21 \pm 1$ °C.

4. Results

4.1. Canonical States of Thermal Convection in the Horizontal Case

Following a logical approach, we start from the simplest case, i.e., the perfectly horizontal configuration ($\vartheta = 0^\circ$) for which convection is expected to emerge in the form of rolls or hexagonal cells according to whether buoyancy or surface-tension effects are dominant, respectively (Rayleigh-Marangoni-Bénard convection). In this regard the first set of figures, collected in Figure 4 for the case with constant liquid depth 0.5 cm, is instructive as these figures show that the pattern-less state visible in the first panel (Figure 4a) is taken over by a recognizable distribution of rolls and localized convective cells as soon as the critical threshold for the onset of convection is exceeded (Figure 4b–d).

These are made evident by the rising (descending) currents of hot (cold) fluid manifesting themselves as localized spots or strips with temperature higher (smaller) than the surrounding fluid.

On increasing the depth of the layer, as expected the horizontal extension of the convective features grows accordingly (compare, e.g., each panel of Figure 5 with the corresponding one in Figure 4). Another key observation stemming from Figure 5 concerns the complexity of the pattern and the number of convective features, which in qualitative agreement with other results in the literature, keep increasing with the ΔT , i.e., grow with the distance from the critical conditions.

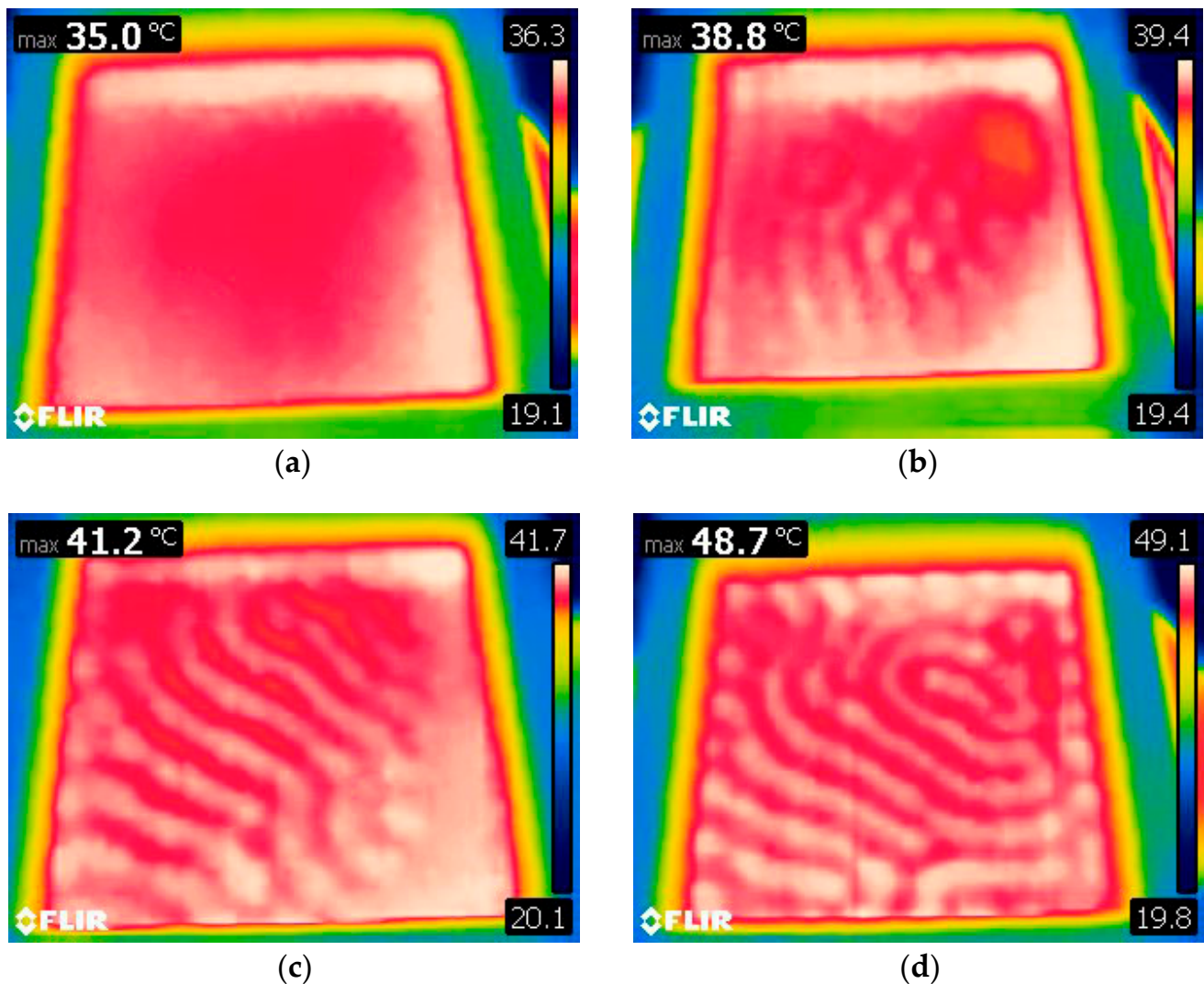


Figure 4. Surface temperature distribution for $d = 0.50$ cm ($\Omega = 32$ mL) and no inclination ($A = 16$, $Bo_{dyn} \cong 0.86$, $Ra \cong 2.5 \times 10^2 \times \Delta T$, $Ma \cong 2.94 \times 10^2 \times \Delta T$): (a) $\Delta T = 13$ °C, (b) $\Delta T = 18$ °C, (c) $\Delta T = 21$ °C, (d) $\Delta T = 27$ °C.

4.2. Convection in Inclined Square Layer

The simplest way to undertake a discussion of the situation where the layer is inclined to the horizontal is to start from the major remark that, unlike the canonical case considered in Section 4.1, for $\vartheta \neq 0$ the basic state is *not in quiescent conditions*. Rather it consists of a *symmetry-breaking shear flow* induced by the horizontal component of the temperature gradient (see the related discussion in the introduction). Put differently, no critical ΔT has to be exceeded in order to induce fluid flow, i.e., convection is produced as soon as a temperature difference is established.

Following up on the previous point, Figure 6 provides a first glimpse of the patterning behavior in such conditions when $\vartheta \cong 3.5^\circ$.

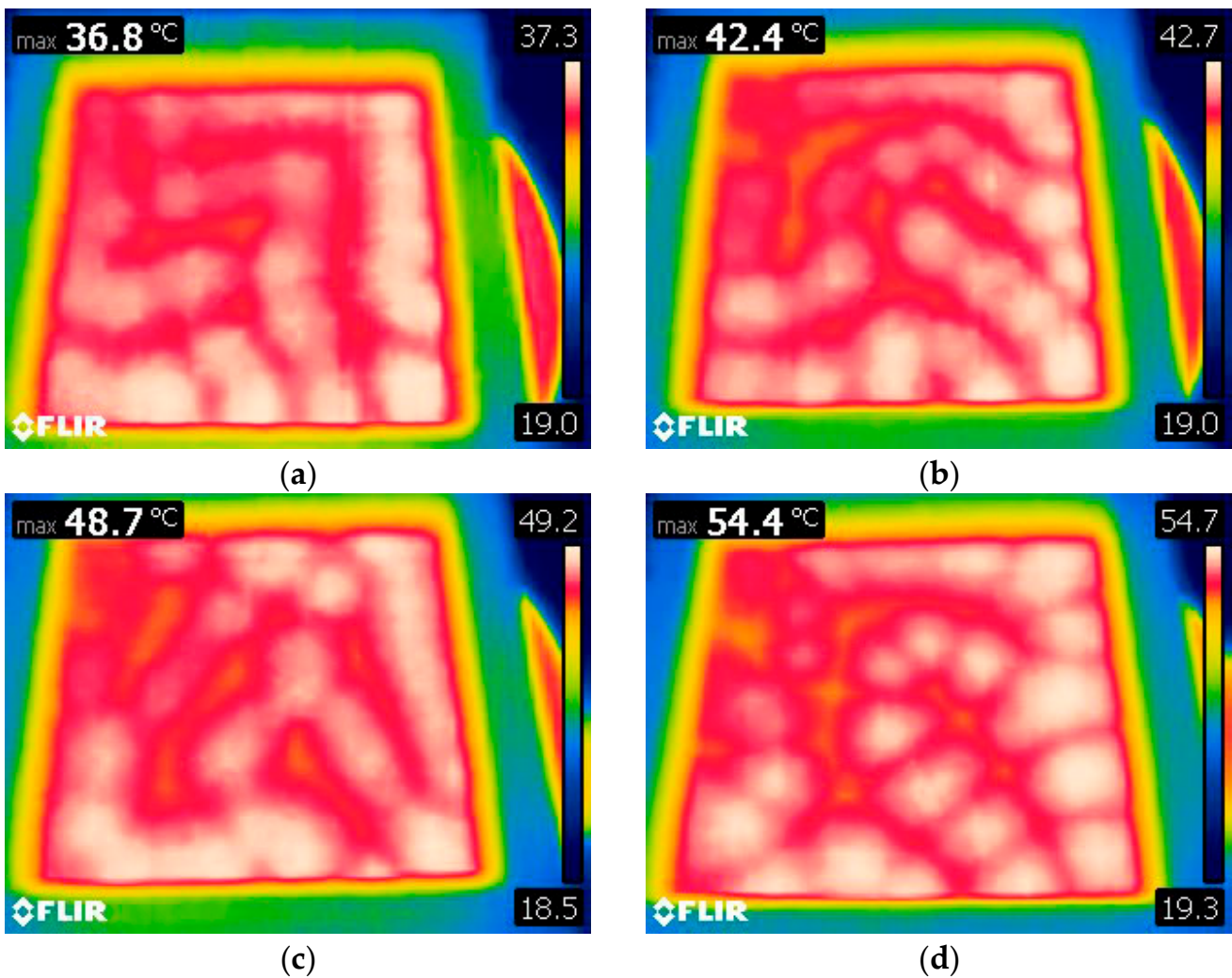


Figure 5. Surface temperature distribution for $d = 0.75$ cm ($\Omega = 48$ mL) ($A = 10.6$, $Bo_{dyn} \cong 1.94$, $Ra \cong 8.6 \times 10^2 \times \Delta T$, $Ma \cong 4.4 \times 10^2 \times \Delta T$): (a) $\Delta T = 15$ °C, (b) $\Delta T = 21$ °C, (c) $\Delta T = 27$ °C, (d) $\Delta T = 33$ °C.

The significance of this figure primarily resides in its ability to make evident that the inclination leads to two remarkable effects. The first concerns the hybrid (spatial) nature of the visible pattern. In place of the scattered distribution of spots occupying all the available space in Figure 4, the surface temperature exhibits in this case an almost feature-free region localized in the part of the physical domain where the depth of the layer is smaller (Figure 6a). Moreover, the random distribution of rolls (in terms of direction in the xz plane) seen in the constant-depth case is taken over by a much more ordered arrangement where the convective features display a tendency to align with the z axis (the vertical direction in the figures, see, e.g., the black dashed lines in Figure 6c).

Notably, although these may immediately be classified as ‘longitudinal rolls’ (their axes being parallel to the tilt direction), their specific spatial configuration bares characteristic ingredients, which also need to be pinpointed suitably here. Their cross-extension, i.e., the typical size in a direction perpendicular to the roll axis undergoes remarkable variations along the z (tilt) direction, which indicates that the dimensional wavelength *is not constant* in the physical domain. Here, this quantity is defined as the distance between two consecutive corresponding crests or “points of the same phase” along the x axis for a fixed value of z . The related behaviors are quantitatively substantiated in Figure 7, where the wavelength has been plotted as a function of the z coordinate for a representative ΔT . Interestingly, as the ΔT is increased, some other interesting changes show up. The length of the rolls along

the z direction grows (compare, e.g., Figure 6a,f, the reader being also referred to the data reported in Figure 8).

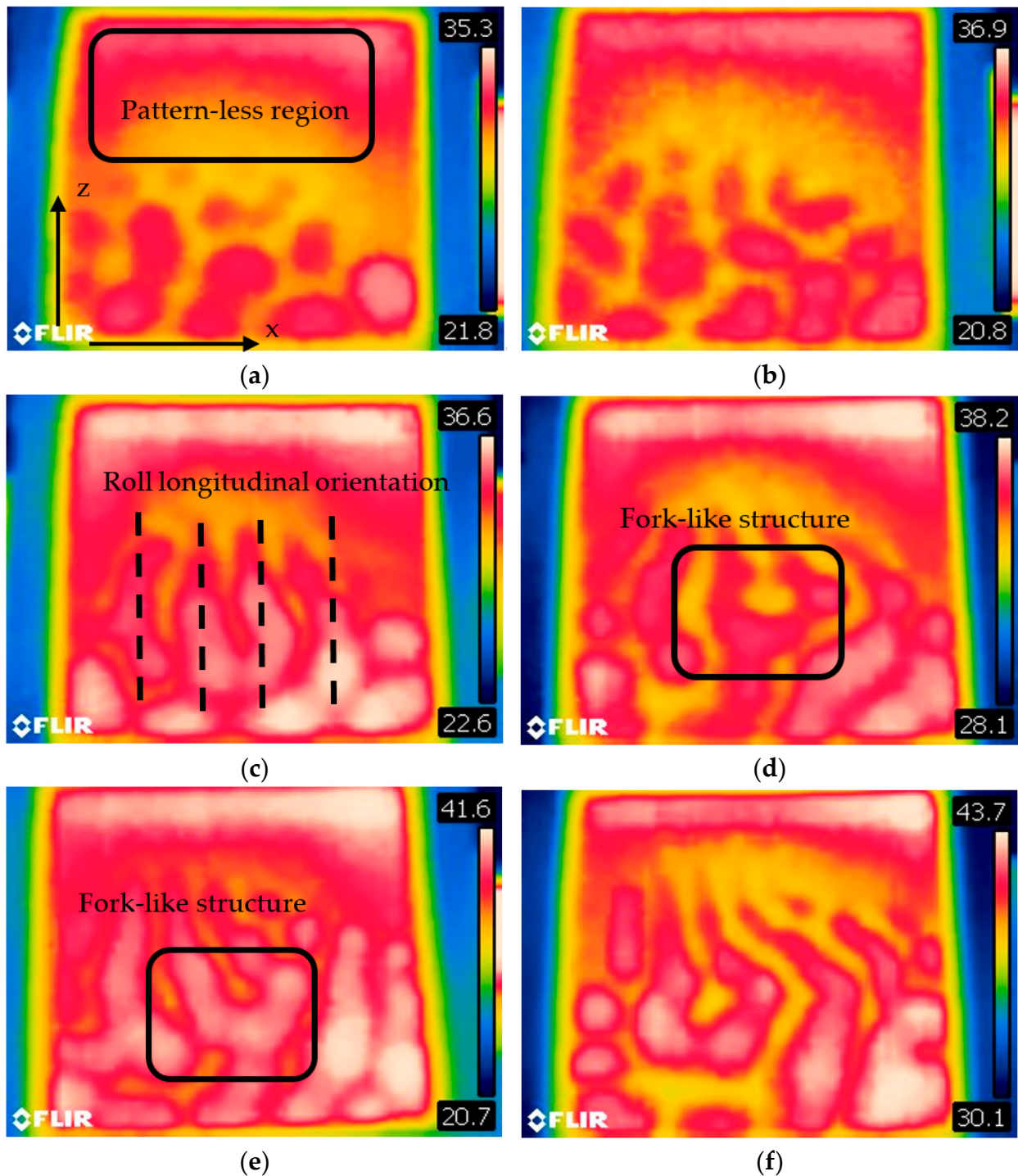


Figure 6. Surface temperature distribution for $d = 0.50$ cm ($\Omega = 32$ mL) and $\vartheta \cong 3.5^\circ$ ($A = 16$, $Bo_{dyn} \cong 0.86$, $Ra \cong 2.5 \times 10^2 \times \Delta T$, $Ma \cong 2.94 \times 10^2 \times \Delta T$): (a) $\Delta T = 15$ °C, (b) $\Delta T = 18$ °C, (c) $\Delta T = 21$ °C, (d) $\Delta T = 24$ °C, (e) $\Delta T = 27$ °C, (f) $\Delta T = 30$ °C (the x and z axes correspond to the horizontal and vertical directions in all the panels).

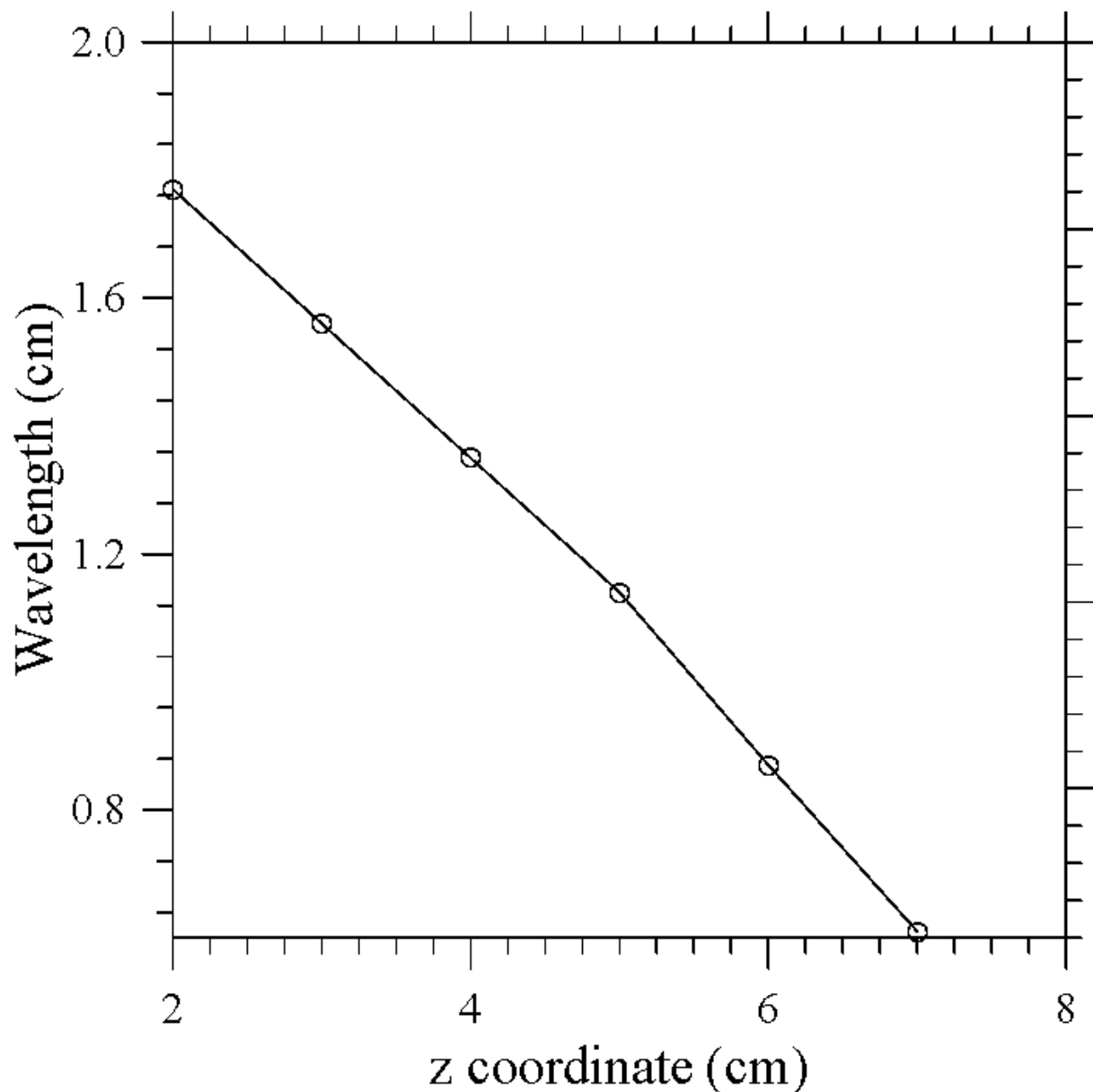


Figure 7. Transverse roll extension as a function of the longitudinal direction z for $\Delta T = 27^\circ\text{C}$ (square container, $A = 16$, $d = 0.50$ cm, $Bo_{dyn} \cong 0.86$, $\vartheta \cong 3.5^\circ$).

Superimposed on these trends, most interestingly, in some cases, in place of the striped pattern, which one would expect in the ideal situations of parallel longitudinal rolls, tree-like shapes can be distinguished in the surface temperature distribution. These give an external observed the illusion of a roll with a fork-like structure (two strips originating from a single initial strip, see the black rectangle in Figure 6d,e).

Given the complexity of such phenomena, which seem to escape a possible simple definition or classification within the framework of the past lines of research (still retaining, however, some affinities with the typical features and salient ingredients pertaining to such categories), in the following, we implement a peculiar modeling and analysis hierarchy in order to ‘filter out’ already known facts and concentrate selectively on new mechanisms. More specifically, this modus operandi is based on the step-by-step variation of the distinct (independent) parameters controlling the various degrees of freedom of the considered system, these being the characteristic temperature ΔT (whose effects have already been outlined before), the tilt angle ϑ , the volume of liquid and the shape and aspect ratio of

the considered container. While the effect of the ΔT has already been outlined before (see gain Figure 8), the overall volume of liquid is expected to influence the dynamics through the related value of the dynamic Bond number based on the average depth of the liquid, which accounts for the relative importance of buoyancy and surface-tension driven effects. Similarly, the shape and aspect ratio of the considered container may influence the pattern selection mechanism through confinement and other geometrical effects.

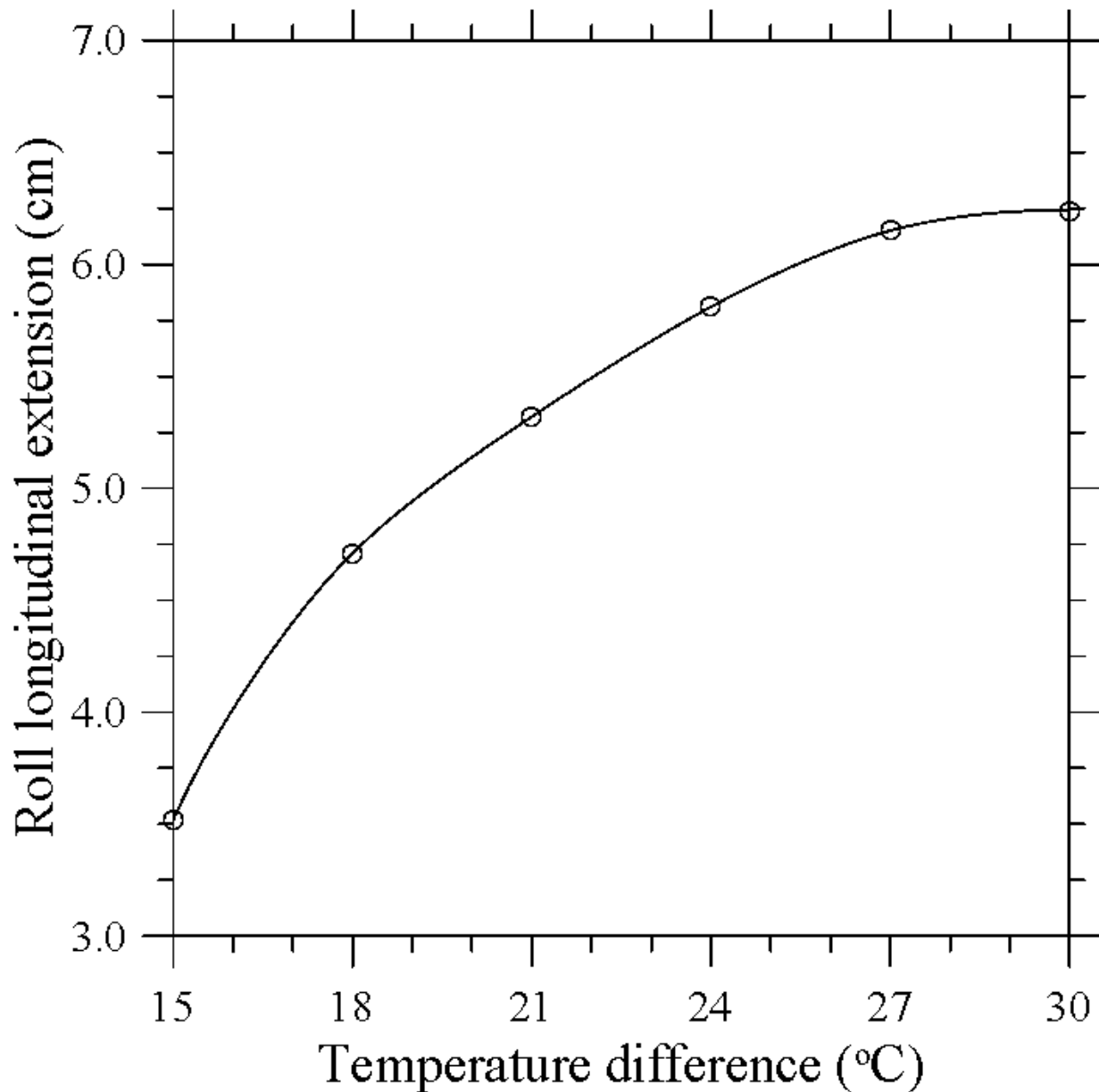


Figure 8. Longitudinal extension of the rolls as a function of ΔT (square container, $A = 16$, $d = 0.50$ cm, $Bo_{dyn} \cong 0.86$, $\vartheta \cong 3.5^\circ$).

As a first step of this analysis hierarchy, we consider a larger value of the inclination angle for the same conditions of Figure 6 (same volume of liquid and set of temperature differences).

As immediately made evident by Figure 9, an increase in ϑ can produce a mitigation of the aforementioned roll pinching mechanism (by which a single longitudinal roll can be split into two neighboring rolls with smaller wavelength). A slightly larger values of ϑ

has also another remarkable consequence; on average, it causes a small (non-negligible) growth of the transverse extension of the rolls (we will return to this effect later).

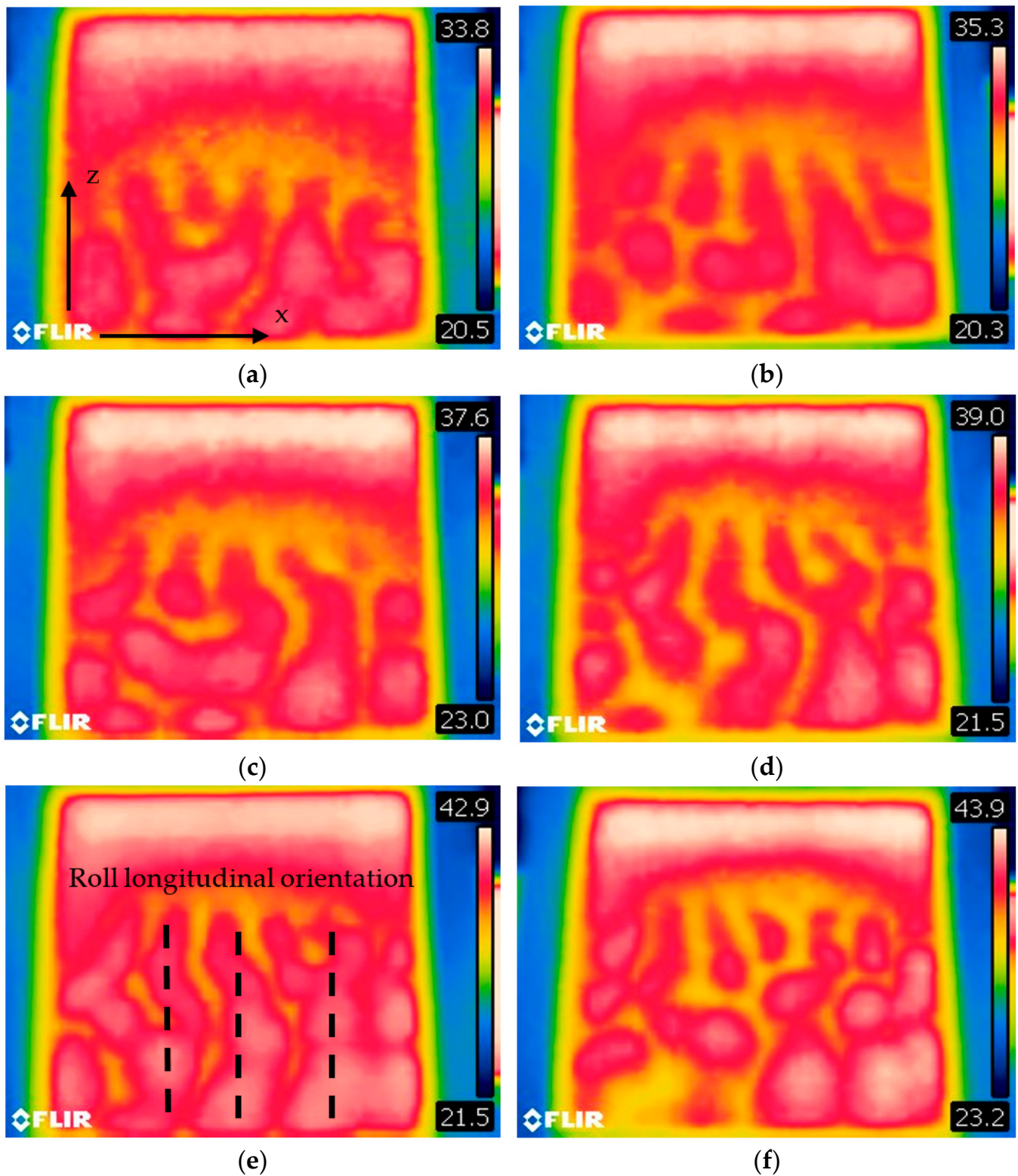


Figure 9. Surface temperature distribution for $d = 0.50$ cm ($\Omega = 32$ mL) and $\vartheta \cong 5^\circ$ ($A = 16$, $Bo_{dyn} \cong 0.86$, $Ra \cong 2.5 \times 10^2 \times \Delta T$, $Ma \cong 2.94 \times 10^2 \times \Delta T$): (a) $\Delta T = 15$ °C, (b) $\Delta T = 18$ °C, (c) $\Delta T = 21$ °C, (d) $\Delta T = 24$ °C, (e) $\Delta T = 27$ °C, (f) $\Delta T = 30$ °C (the x and z axes correspond to the horizontal and vertical directions in all the panels).

The reduced tendency of the system to support roll pinching mechanism is qualitatively substantiated in Figure 10. On closer inspection, indeed, this figure reveals that the number of peaks visible at each station z remains almost constant throughout the longitudinal extension of the domain (until no well-defined peaks can be seen as a certain limiting value of z is exceeded, which corresponds to the transition from the patterned to the spot-free region).

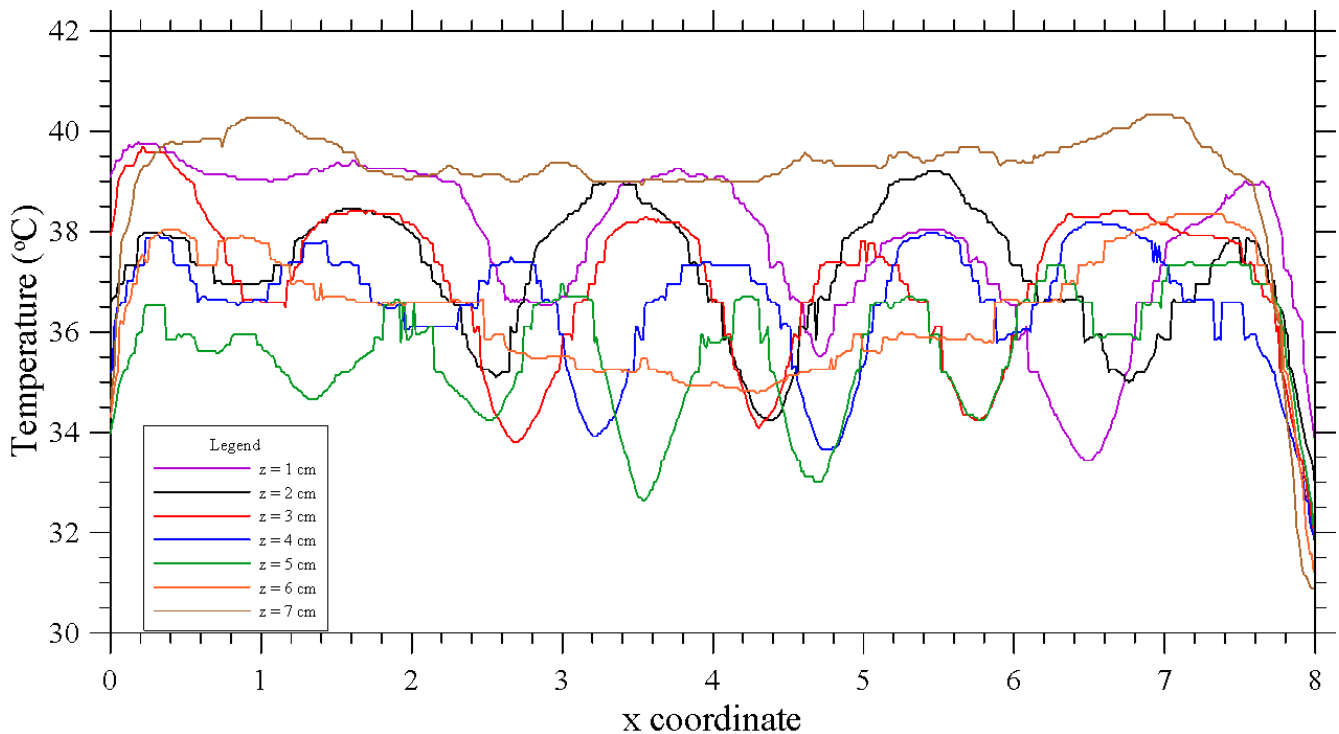


Figure 10. Profiles of temperature at different stations along the longitudinal direction z (square container, $A = 16$, $d = 0.50$ cm, $Bo_{dyn} \cong 0.86$, $\Delta T = 27^\circ\text{C}$, $\vartheta \cong 5^\circ$).

Towards the end of getting a better grasp on how all these dynamics are affected by the depth of the layer, the next set of figures refers to the case where the average depth of the liquid is 0.75 cm (see Figure 11, yet for $\vartheta \cong 5^\circ$). Along these lines, taken together Figures 9 and 11 are instrumental in showing that an increase in the relative importance of buoyancy forces with respect to surface-tension driven effects (as witnessed by the related rise in the dynamic Bond number) can help to make the roll-pinching mechanism even less frequent in favor of a more regular (parallel) distribution of longitudinal rolls. As even a fleeting glimpse into Figure 11 would immediately reveal, in fact, the patterned surface now corresponds to the entire free liquid-gas interface of the fluid layer, i.e., no cell-free area can be identified in this case (a kind of “saturated state” is attained in terms of roll extension along the tilt direction z).

Additional insights follow naturally from a cross-comparison of Figures 10 and 12. It can be seen that the number of rolls sitting in the cavity is reduced in the $d = 0.75$ cm case (as clearly demonstrated by the smaller number of recognizable peaks at any given station in comparison to the equivalent ones visible in Figure 10 for $d = 0.5$ cm).

All these trends are finally summarized in Figure 13 in terms of roll extension along x as a function of the longitudinal coordinate z for different values of the layer average depth and inclination.

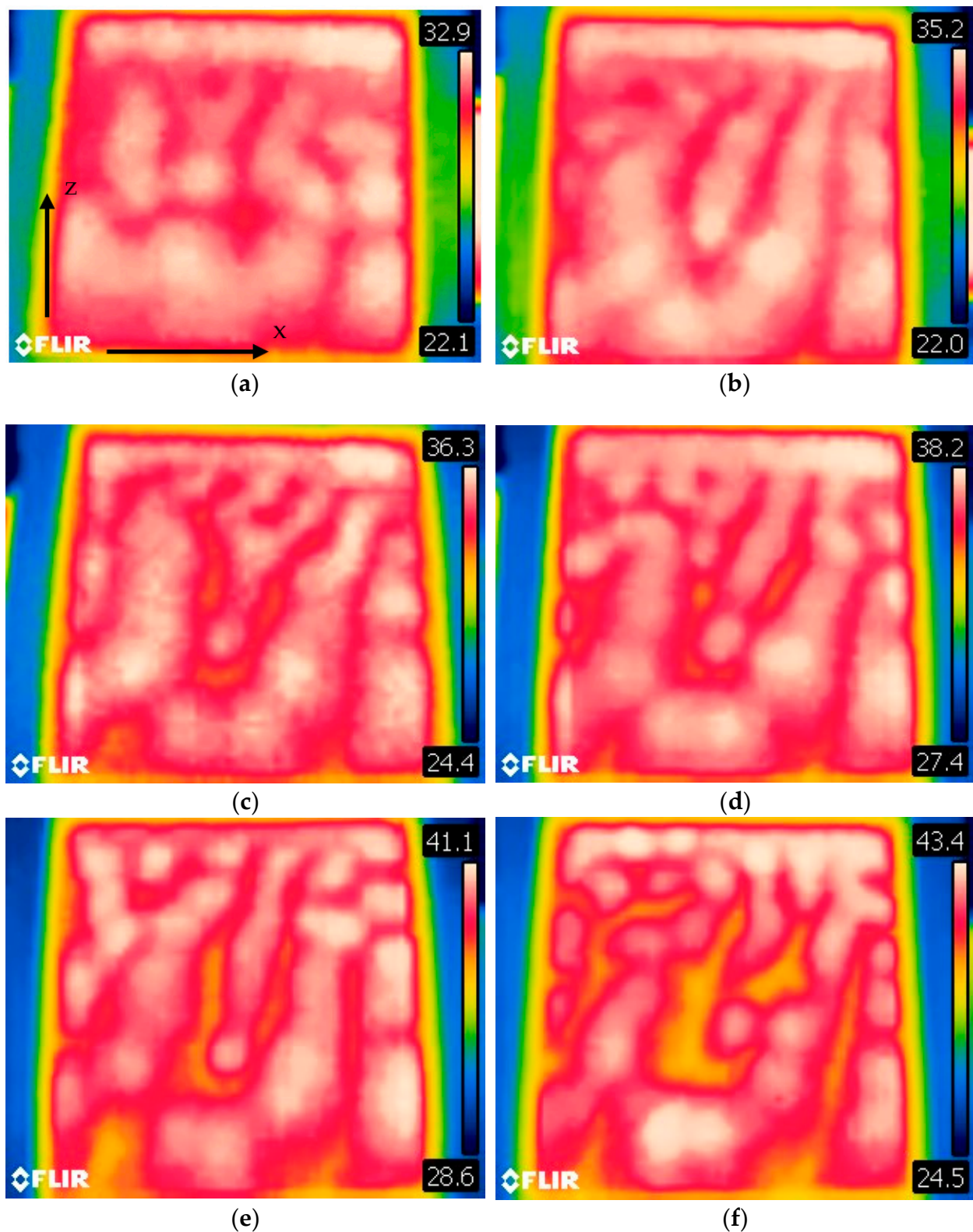


Figure 11. Surface temperature distribution for $d = 0.75$ cm ($\Omega = 48$ mL) and $\vartheta \cong 5^\circ$ ($A = 10.6$, $Bo_{dyn} \cong 1.94$, $Ra \cong 8.6 \times 10^2 \times \Delta T$, $Ma \cong 4.4 \times 10^2 \times \Delta T$) (a) $\Delta T = 15$ °C, (b) $\Delta T = 18$ °C, (c) $\Delta T = 21$ °C, (d) $\Delta T = 24$ °C, (e) $\Delta T = 27$ °C, (f) $\Delta T = 30$ °C (the x and z axes correspond to the horizontal and vertical directions in all the panels).

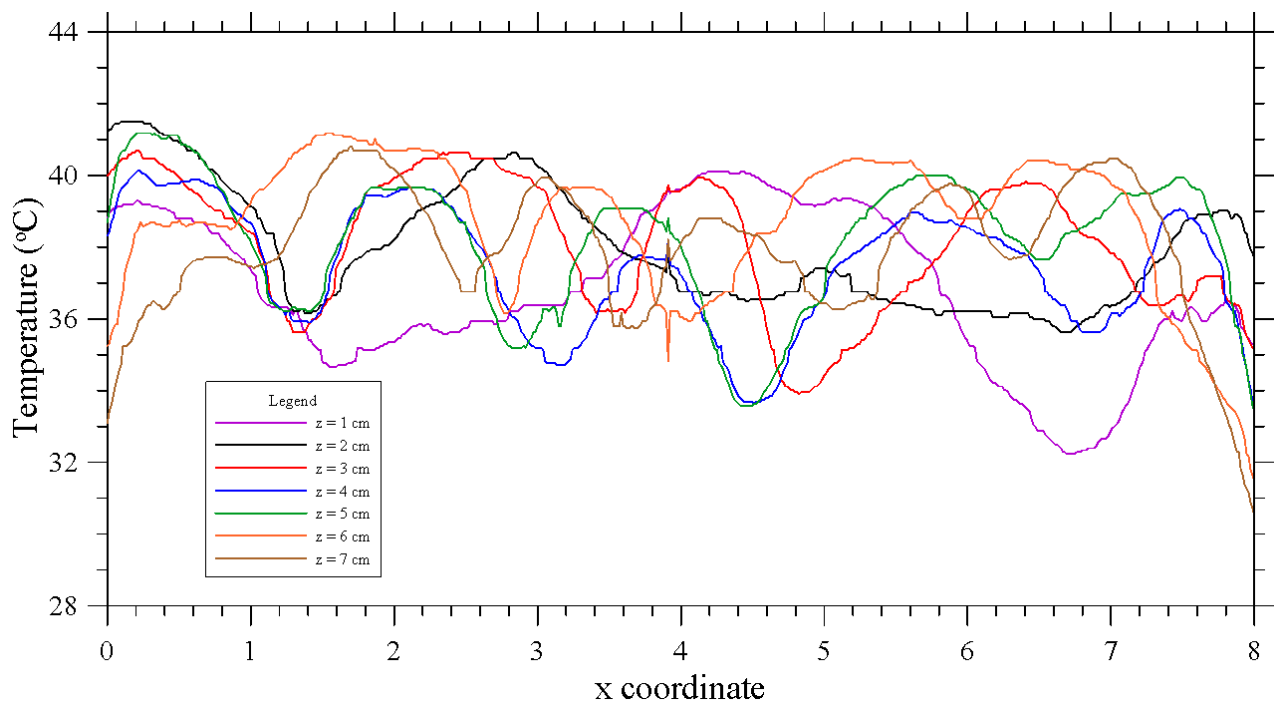


Figure 12. Profiles of temperature at different stations along the longitudinal direction z (square container, $A = 10.6$, $d = 0.75$ cm, $Bo_{dyn} \cong 1.94$, $\Delta T = 27$ °C, $\vartheta \cong 5^\circ$).

Having completed a description of the observed phenomena in the square geometry case, we now turn to considering briefly the equivalent dynamics emerging in the cylindrical container. As already explained to a certain extent before, this practice finds its justification in the two-fold purpose of assessing the role played by the system aspect ratio (ratio of the horizontal and average vertical extension) and the shape of the side boundary.

4.3. Convection in Inclined Cylindrical Layer

As the reader will immediately realize by inspecting Figure 14, moving on from the case with square boundary to that with cylindrical sidewall (compare with Figure 6), no significant or appreciable changes can be discerned in terms of patterning behavior. The flow still displays a set of coexisting rolls, which originate from the side where the fluid depth is larger and protrude into the pattern-less region located at the other end of the container.

Although from a qualitative standpoint, the scenario is essentially the same, however, a discrepancy or departure from the equivalent dynamics shown in Figure 6 can be identified. It is represented by the tendency of the rolls to assume an *oblique configuration* with respect to the tilt direction (North-West/South-East in the different panels of Figure 14, see, e.g., the black dashed lines in Figure 14c,f).

Moreover, as revealed by a closer (quantitative) assessment of the pattern in terms of wavelength, this difference in the prevailing roll orientation occurs in conjunction with an appreciable increase in the roll transverse extension (Figure 15).

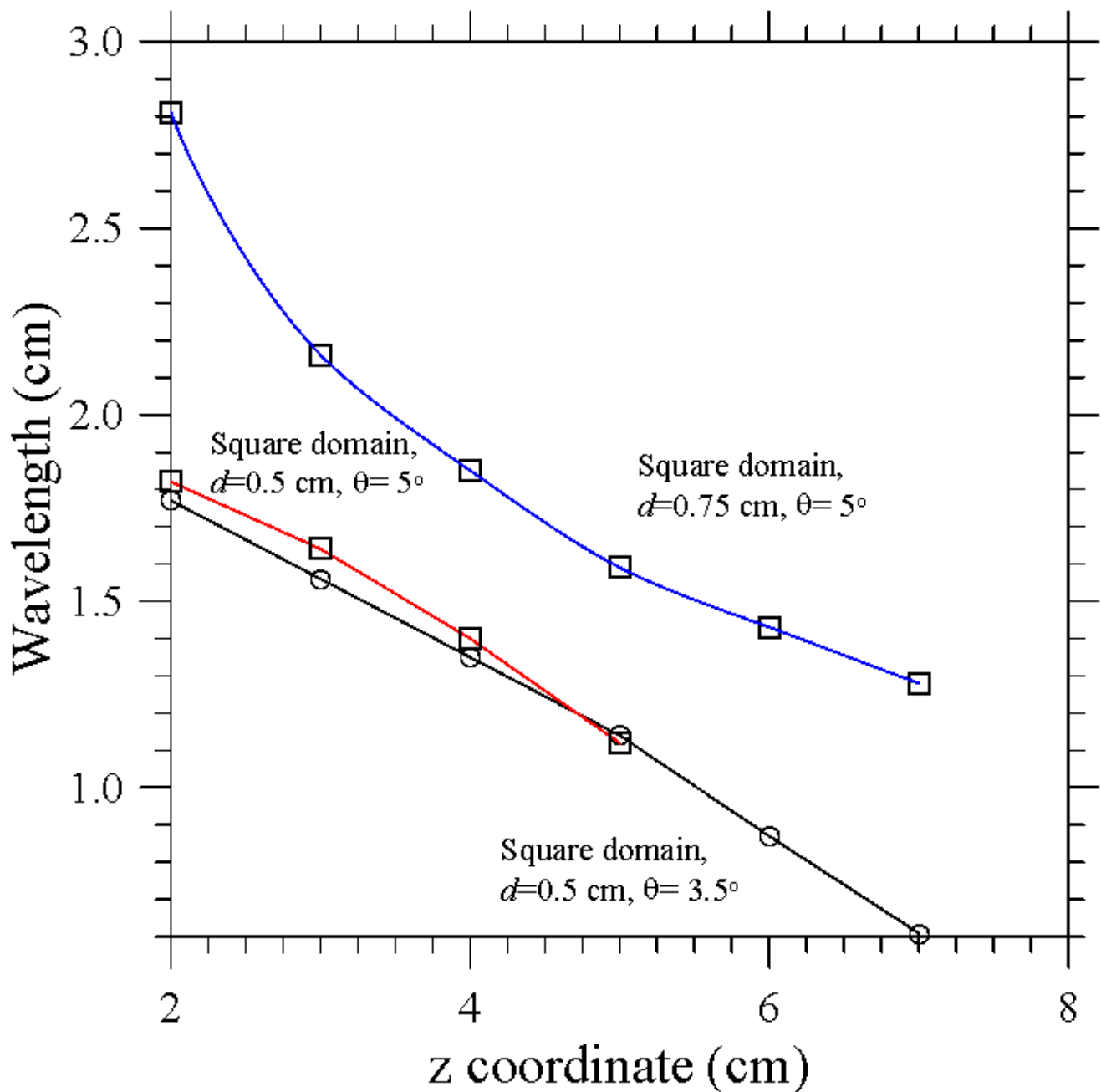


Figure 13. Transverse roll extension as a function of the longitudinal direction z for $\Delta T = 27^\circ\text{C}$ for different average fluid depths and inclinations (square container).

On the one hand, these results indicate that the scenario does not depend significantly on the shape of the domain, on the other hand, they provide evidence that, if the geometrical aspect ratio is increased ($A = 26.6$ as opposed to $A = 16$), the pattern is allowed to “relax” in the horizontal direction, thereby causing an increase in the dimensional wavelength. Another (more obvious) outcome of the cylindrical nature of the outer solid boundary is the modulation of the longitudinal extension of the rolls along the x axis for any fixed value of ΔT (the rolls closer to left and right side of the container having smaller longitudinal extension than those located in the center).

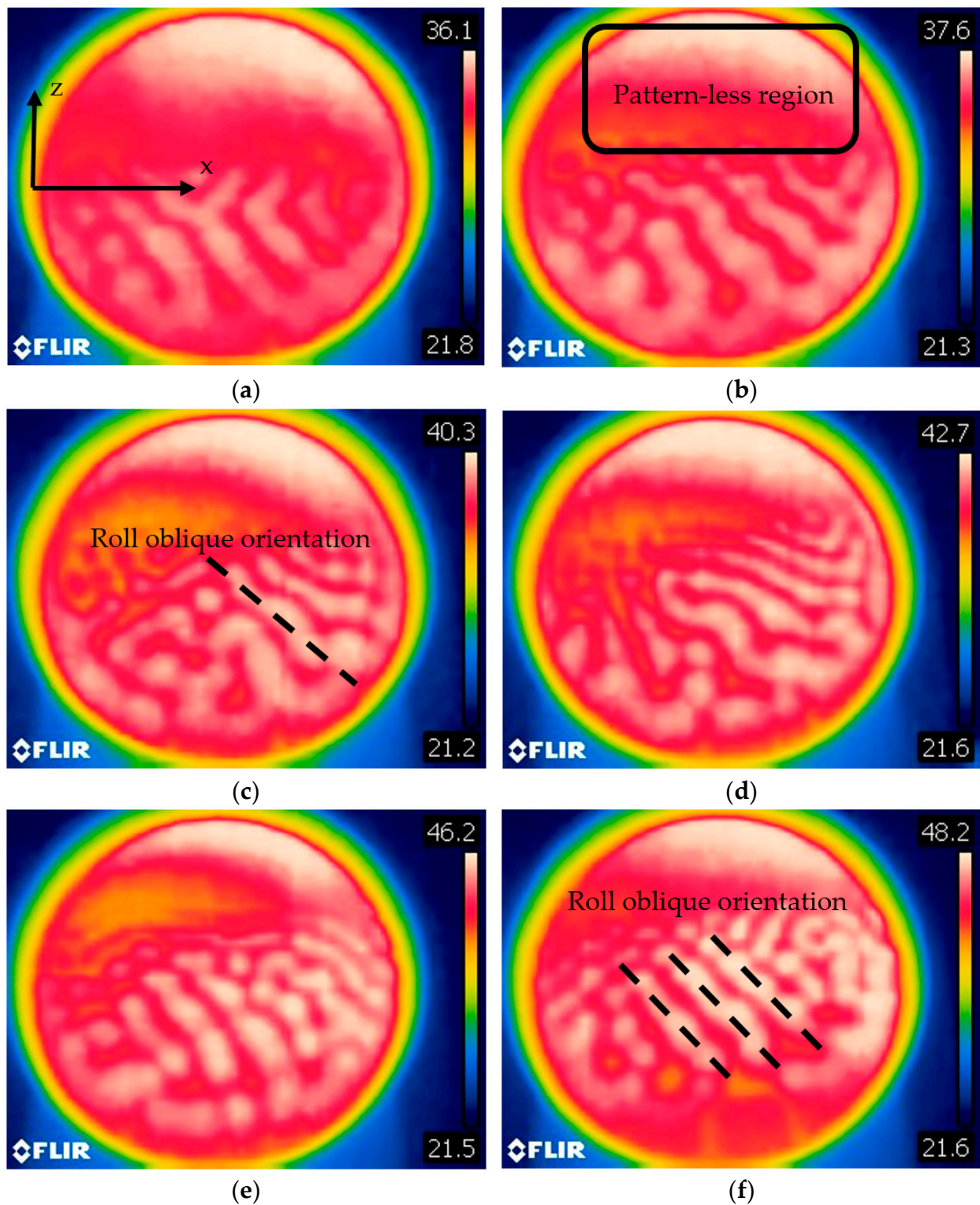


Figure 14. Surface temperature distribution for $d = 0.50$ cm ($\Omega \cong 70$ mL) and $\vartheta \cong 3.5^\circ$ ($A = 26.6$, $Bo_{dyn} \cong 0.86$, $Ra \cong 2.5 \times 10^2 \times \Delta T$, $Ma \cong 2.94 \times 10^2 \times \Delta T$): (a) $\Delta T = 15$ °C, (b) $\Delta T = 18$ °C, (c) $\Delta T = 21$ °C, (d) $\Delta T = 24$ °C, (e) $\Delta T = 27$ °C, (f) $\Delta T = 30$ °C (the x and z axes correspond to the horizontal and vertical directions in all the panels).

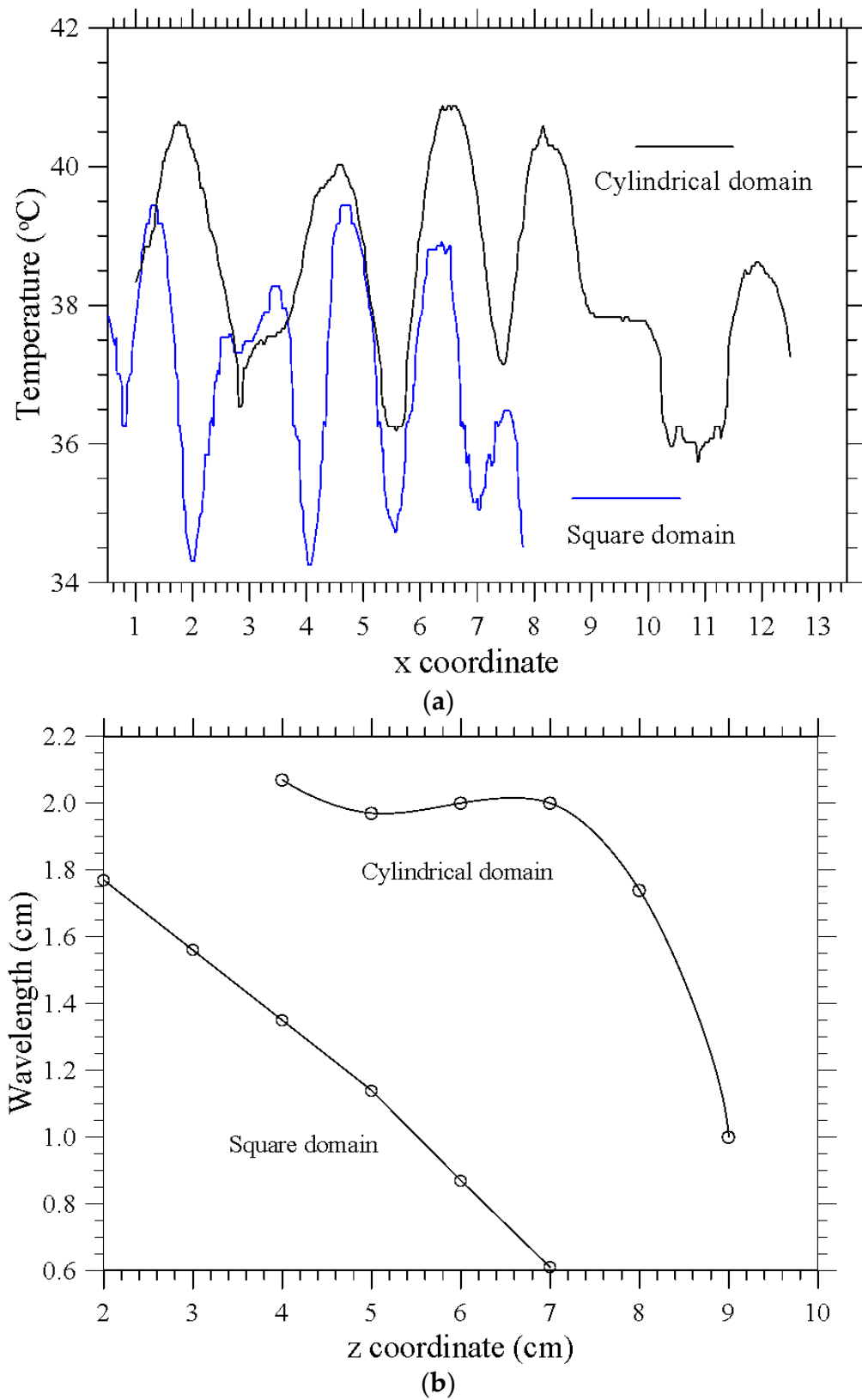


Figure 15. Transverse roll extension analysis ($d = 0.50$ cm, $Bo_{dyn} \cong 0.86$, $\Delta T = 27$ °C, $\vartheta \cong 3.5^\circ$): (a) Temperature as a function of the transverse coordinate x at $z = 4$ cm, (b) Roll extension along x as a function of the longitudinal direction z .

Figure 16 naturally complements Figure 14, where additional evidence is provided that, on increasing the inclination, the transverse wavelength can be made higher (especially for intermediate values of z).

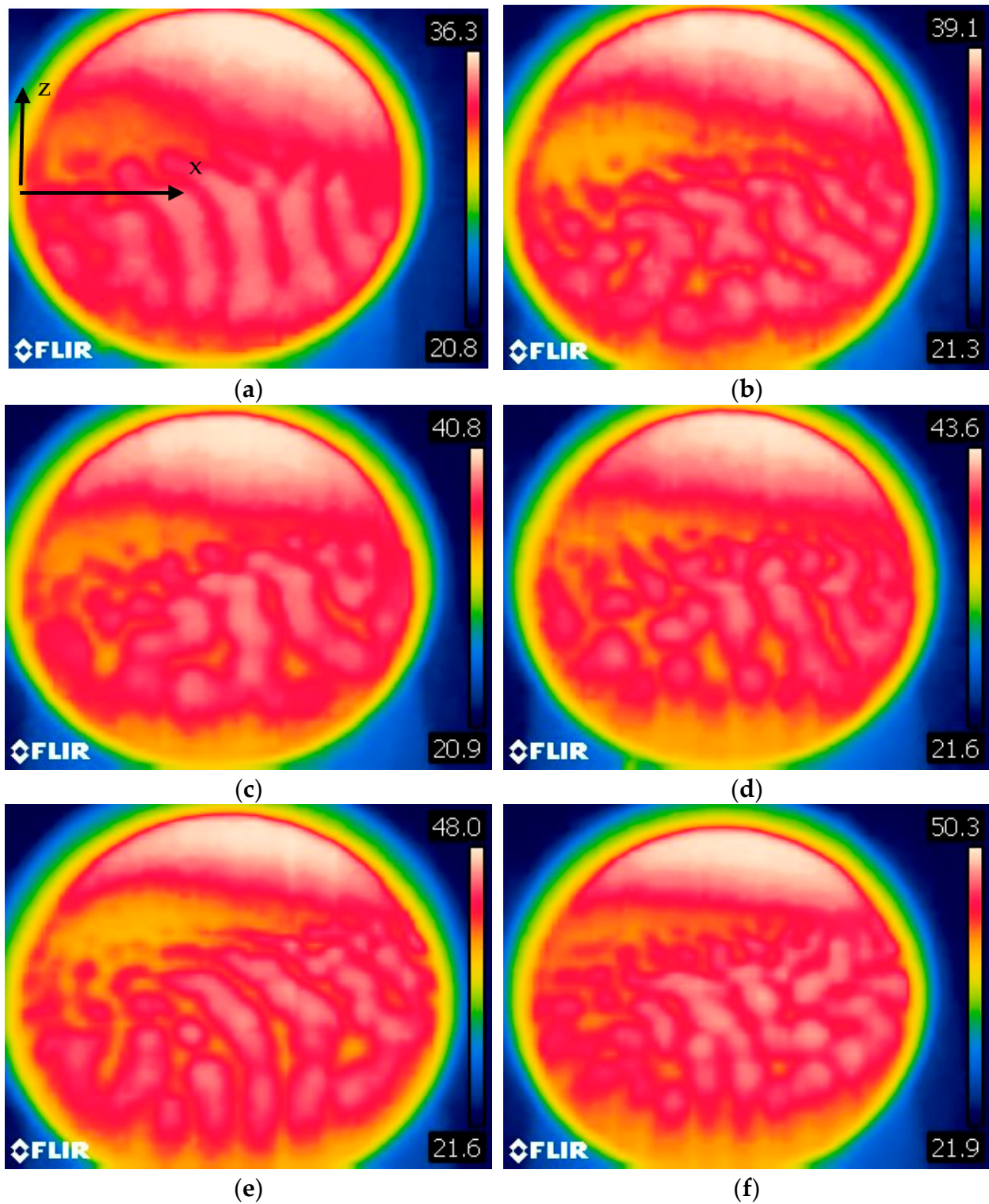


Figure 16. Surface temperature distribution for $d = 0.50$ cm ($\Omega \cong 70$ mL) and $\vartheta \cong 5^\circ$ ($A = 26.6$, $Bo_{dyn} \cong 0.86$, $Ra \cong 2.5 \times 10^2 \times \Delta T$, $Ma \cong 2.94 \times 10^2 \times \Delta T$): (a) $\Delta T = 15$ °C, (b) $\Delta T = 18$ °C, (c) $\Delta T = 21$ °C, (d) $\Delta T = 24$ °C, (e) $\Delta T = 27$ °C, (f) $\Delta T = 30$ °C (the x and z axes correspond to the horizontal and vertical directions in all the panels).

Figures 17 and 18 complete this sequence by illustrating the behavior for larger average depth of the layer (Figure 18 to be compared for analogous circumstances with the findings about the square layer in Figure 11).

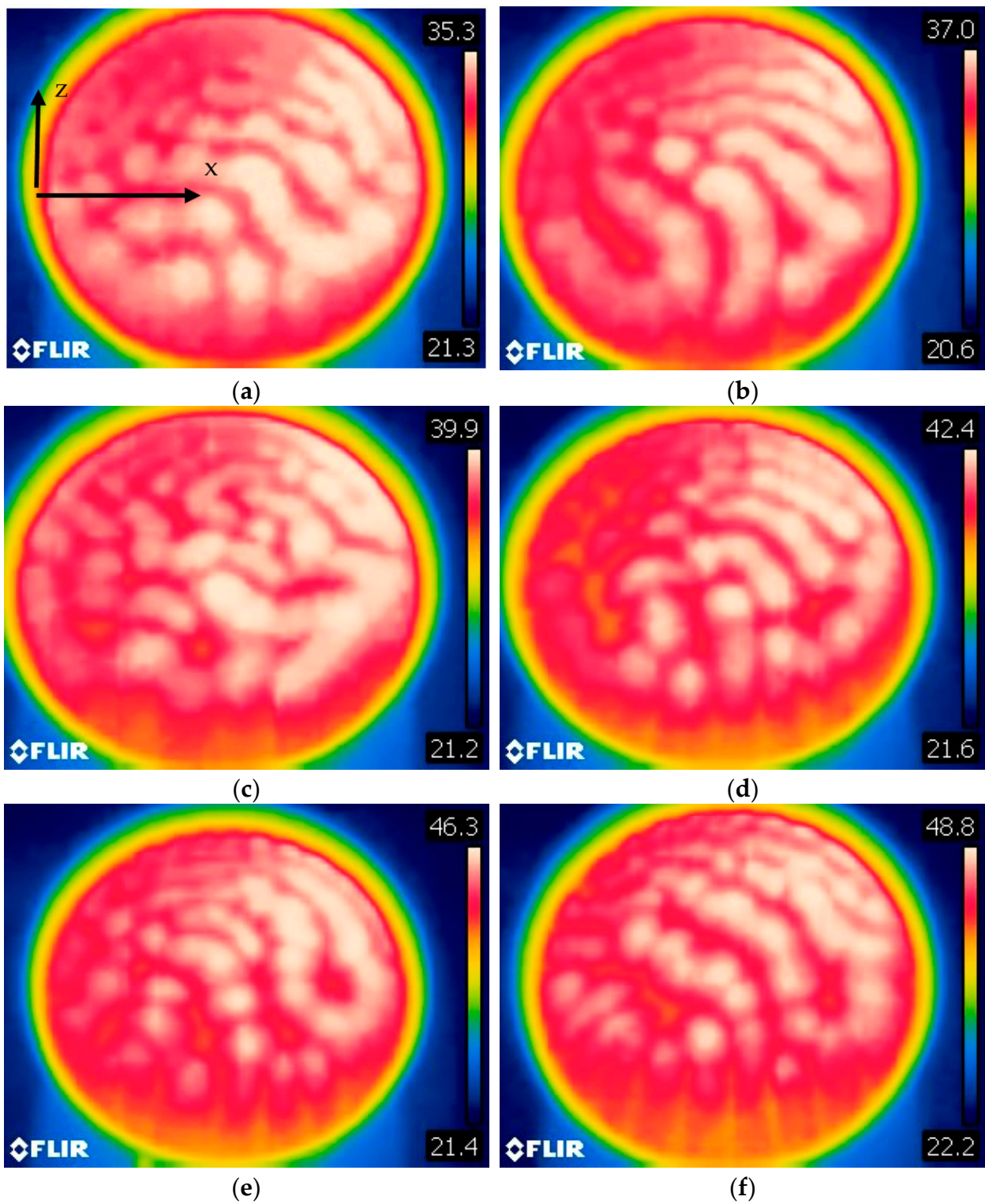


Figure 17. Surface temperature distribution for $d = 0.75$ cm ($\Omega = 104$ mL) and $\vartheta \cong 3.5^\circ$ ($A = 17.7$, $Bo_{dyn} \cong 1.94$, $Ra \cong 8.6 \times 10^2 \times \Delta T$, $Ma \cong 4.4 \times 10^2 \times \Delta T$) (a) $\Delta T = 15^\circ\text{C}$, (b) $\Delta T = 18^\circ\text{C}$, (c) $\Delta T = 21^\circ\text{C}$, (d) $\Delta T = 24^\circ\text{C}$, (e) $\Delta T = 27^\circ\text{C}$, (f) $\Delta T = 30^\circ\text{C}$ (the x and z axes correspond to the horizontal and vertical directions in all the panels).

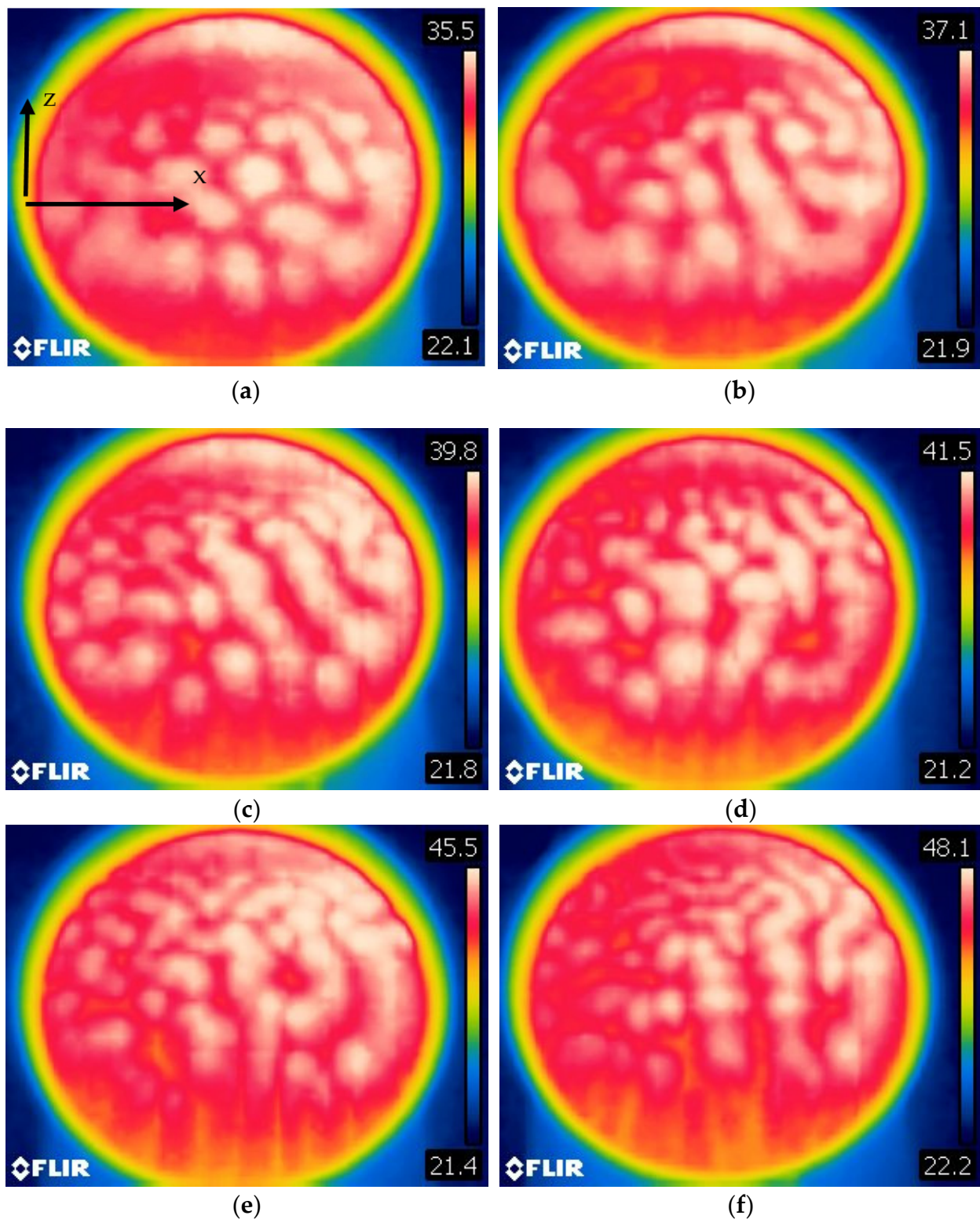


Figure 18. Surface temperature distribution for $d = 0.75$ cm ($\Omega = 104$ mL) and $\vartheta \cong 5^\circ$ ($A = 17.7$, $Bo_{dyn} \cong 1.94$, $Ra \cong 8.6 \times 10^2 \times \Delta T$, $Ma \cong 4.4 \times 10^2 \times \Delta T$) (a) $\Delta T = 15$ °C, (b) $\Delta T = 18$ °C, (c) $\Delta T = 21$ °C, (d) $\Delta T = 24$ °C, (e) $\Delta T = 27$ °C, (f) $\Delta T = 30$ °C (the x and z axes correspond to the horizontal and vertical directions in all the panels).

Figure 19 finally provides an ensemble perspective on the system response for all the cases considered in Sections 4.2 and 4.3. A number of interesting functional dependences can be discerned accordingly. In addition to the aforementioned tendency of the transverse wavelength to attain larger values as the inclination and/or the liquid average depth (volume) are increased (with the values for the cylindrical domain being generally located above the corresponding ones for the square container with smaller aspect ratio), some interesting non-monotonic behaviors can be spotted there.

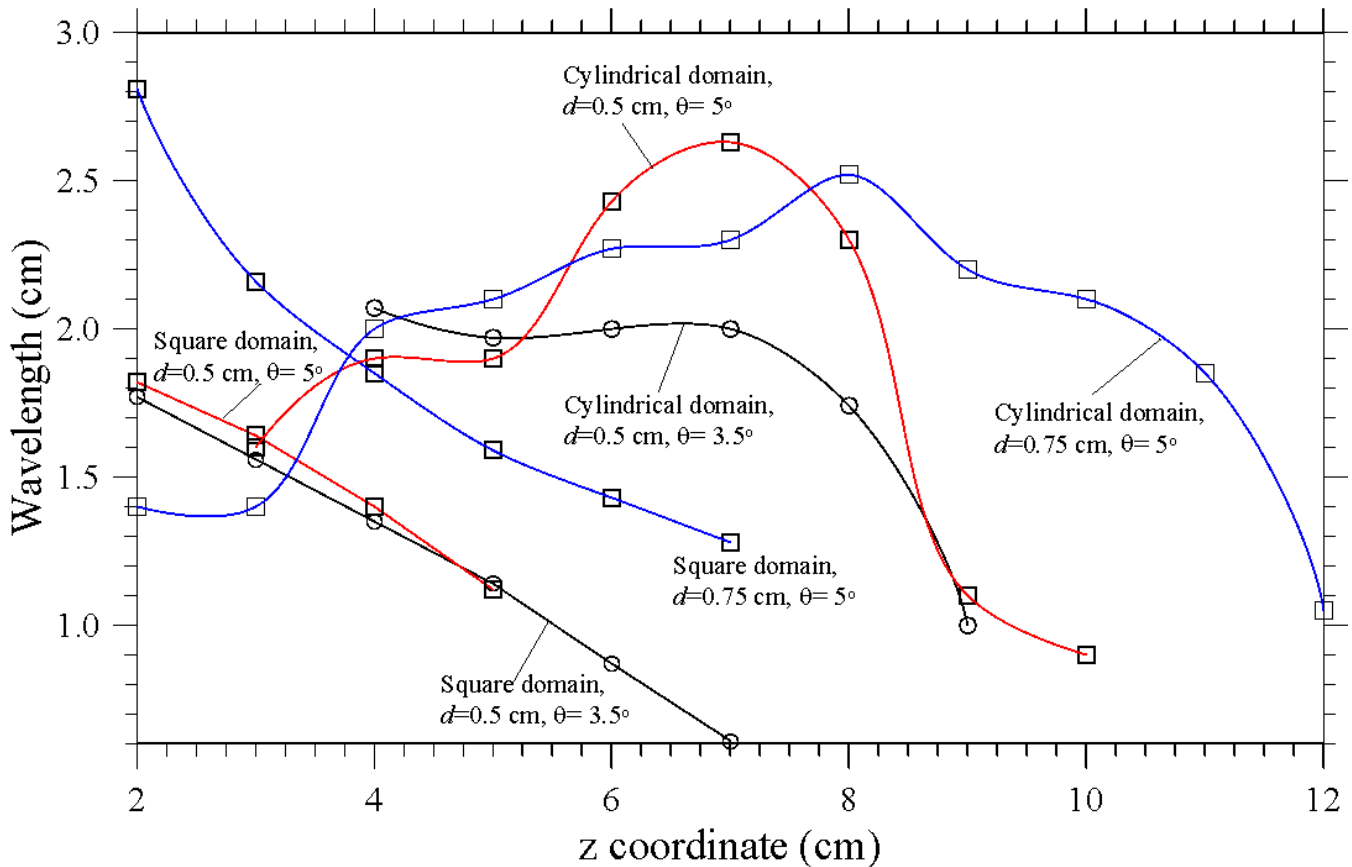


Figure 19. Transverse roll extension as a function of the longitudinal direction z for all the cases considered in the present work ($\Delta T = 27^\circ\text{C}$).

In the cylindrical case, for $d = 0.5\text{ cm}$ ($Bo_{dyn} \cong 0.86$) and $\vartheta \cong 5^\circ$ the wavelength curve is entirely located above the corresponding one for the square domain (refer to the red branches in Figure 19). The cylindrical case, however, displays a maximum for $z = 7\text{ cm}$, followed by a branch of decreasing behavior. Notably, an interval of the z coordinate can be identified accordingly where the wavelength for $\vartheta \cong 5^\circ$ is smaller than that attained for the same average liquid depth ($d = 0.5\text{ cm}$) and $\vartheta \cong 3.5^\circ$ ($z < 5.2\text{ cm}$). The same concept applies to the curve for $d = 0.75\text{ cm}$ ($Bo_{dyn} \cong 1.94$) and $\vartheta \cong 5^\circ$. Although, the wavelength is larger than the corresponding one for $d = 0.5\text{ cm}$ over almost the entire longitudinal extension of the fluid domain, this relationship is inverted in the range $5.7 < z < 7.7\text{ cm}$. This curve even intersects the corresponding one for the square container for $z \cong 3.8\text{ cm}$ (refer to the blue branches in Figure 19), which indicates that circumstances exist where the wavelength in the cylindrical case can become smaller than the equivalent square-domain value ($Bo_{dyn} \cong 1.94$, $\vartheta \cong 5^\circ$ and $z < 3.8\text{ cm}$).

5. Discussion

It is a well-known concept that, regardless of whether the underpinning processes are different or not, systems that are driven out of equilibrium often display similar behaviors or patterns (Lappa [11]). To put the present work in perspective, therefore, in this section some effort is provided to emphasize on some prior research displaying some potential links with the results described in Section 4. In other words, we sift through existing studies with different foci in order to glean hints and draw inferences about possible affinities in terms of underlying mechanisms with the present phenomena.

In particular, in our endeavor to do so, the discussion is articulated along two different threads. Namely, first, we consider the existing literature on surface-tension driven convection in horizontal layers with inclined temperature gradient and then we review the existing studies on pure gravitational convection in inclined shallow enclosures with constant depth (geometries with a rectangular transverse section).

In the former case, some commonality can be seen the existence of a symmetry breaking shear flow, which can deeply influence the effective patterning behavior. A detailed classification of the fundamental modes of surface-tension-driven convection developed by horizontal layers with an inclined temperature gradient can be found in the linear stability analysis by Nepomnyashchy et al. [33], where these were categorized as stationary longitudinal rolls (LR) essentially driven by the same thermal effects that can produce classical MB convection and transverse rolls for which shear plays a much more important role (manifesting as traveling entities through the layer). Hydrothermal waves (HTW) were also identified in the case for which the horizontal component of the temperature gradient becomes so strong that it can hinder the concurrent mechanisms driven by the vertical component (this being the opposite extreme case with respect to that where the vertical component of the temperature gradient is dominant, thereby producing the classical MB hexagonal cells).

Due to the lack of HTWs in the present case even in the situation for which the depth of the layer is minimal (Figures 6, 9, 14 and 16), we infer that the present conditions are far from those for which these specific modes of convection can be excited. Another possible explanation could be rooted in another class of studies dealing with hybrid Marangoni-buoyancy convection in differentially heated liquid layers (the gradient of temperature being parallel to the free interface in this case). Evidence has been provided in the literature that if buoyancy is sufficiently strong in comparison to surface-tension driven effects, the HTW (which would represent the preferred mode of supercritical Marangoni convection) is taken over by longitudinal rolls with axes parallel to the (horizontal) temperature gradient. Relevant examples of related findings can be found in the experimental studies by Gillon and Homsy [45], Braunsfurth, and Homsy [46], Burguete et al. [47] and Pelacho et al. [48], to which the interested reader is referred for additional details.

In such a context, another work deserving a quote is that by Shklyaev and Nepomnyashchy [35]. These authors shed additional lights on the pure Marangoni-flow case with inclined temperature gradient by gaining relevant information about the effective morphology of the emerging convection structures through non-linear numerical simulations. For a sample liquid with $Pr = 7$, they could determine the morphological changes undergone by the compact cells typical of MB convection under the effect of a superimposed shear flow (leading to cells that “drift” in the physical domain) and show that between the areas of the existence of the hexagonal patterns and the longitudinal rolls (obtained for a horizontal temperature gradient larger than that needed to produce the drifting cells), there is a stability domain of “oblique rolls”, i.e., rolls inclined with respect to the direction of the horizontal temperature gradient. Most interestingly, they also found states with half of the convective pattern consisting of oblique rolls with positive inclination angle and the other half displaying rolls with a negative inclination angle of the same modulus.

Yet, for the case with inclined temperature gradient, Ueno et al. [34] were the first to report on stationary longitudinal rolls and drifting cells by means of experiments with layers of silicone oils with viscosity 2, 5, 10 and 20 cSt ($Pr = 27.9, 67.0, 111.9$ and 206.8 at room temperature, respectively) up to 2 [mm] in depth. Later, Mizev and Schwabe [3] conducted an experimental campaign to assess the role played in such dynamics by the depth of the layer (10 cSt silicone oil with a thickness d varying from 1.0 to 6.0 mm). These authors found that as the layer thickness increases the Marangoni–Bénard cells elongate along the direction of thermocapillary motion. Finally, when the longitudinal size of the cells reaches the horizontal size of the layer, a new flow structure appears in the form of LR. More precisely, they observed that for any depth of the layer in the considered range, while an increase in the horizontal component of the temperature gradient for a fixed vertical contribution can cause a transition from drifting cells to LR, vice versa, an increase in the vertical component of the temperature gradient for a fixed horizontal contribution leads to the opposite transition.

Although several analogies might be identified between these behaviors and the present findings, we should recall at this stage that in the present case, in addition to the inclination of the temperature gradient with respect to the free interface, the depth of the liquid layer is not constant.

Moreover, drawing a parallelism with the existing findings for surface-tension driven convection may not be exhaustive because buoyancy should be expected to play a significant role in the situations considered here for which $Bo_{dyn} > 1$. Along these lines, a critical analysis of the existing literature for pure buoyancy flow in inclined shallow enclosures (no free interface) might also lead to interesting insights.

The simplest way to do so, perhaps, is to start from the simple remark that for inclined systems subjected to buoyancy only and relatively small angles of inclination such as those considered in the present work, these systems tend to develop stationary longitudinal rolls (LR), i.e., rolls of essentially buoyant nature that aligns with the direction of the shear flow are the typical outcome of the primary instability of these systems. Only if the inclination angle is relatively large, the ground is left to transverse rolls (TR), i.e., rolls with axes perpendicular to the shear flow essentially driven by shear (Chen and Pearlstein [23]). Fujimura and Kelly [26] clarified that the transition angle essentially depends on the Prandtl number of the considered fluid and it is less than 90° only if the Prandtl number is smaller than 12.47 (Fujimura and Kelly [26]), which implicitly leads to the conclusion that LR should be regarded as the primary pattern forming process in oils and other fluids with relatively large values of the Prandtl number.

The present findings (see, in particular, Figure 11 for the case in which buoyancy is dominant) confirm that such a trend (i.e., the tendency to favor LR for small tilt angles) still holds although situations with non-constant depth of the layer have been considered.

Remarkably, Figures 17 and 18 also provide a hint or clue for another interesting connection or affinity with the dynamics described in the studies by Shadid and Goldstein [24] and Busse and Clever [25]. In this regard, it is worth recalling that the former authors could observe experimentally in the case of a fluid with $Pr = 90$ (reagent grade ethylene glycol) that, for low to moderate angles of inclination and a sufficiently high value of the Rayleigh number, the longitudinal rolls can become unstable against a three-dimensional “wavy” instability (in line with the predictions of the linear stability analysis by Clever and Busse [22]). Two instability mechanisms were revealed accordingly, i.e., an instability of the cross-roll type, by which a disturbance perpendicular to the original roll axis is produced, and a pinching process able cause coalescence of adjacent rolls. Apart from these steady-rolls wavelength-changing mechanism, Shadid and Goldstein [24] also reported on unsteady longitudinal rolls taking over for $Ra > 10^4$ over the interval $5 \leq \theta \leq 25^\circ$. By means

of numerical simulations, Busse and Clever [25] could confirm that a three-dimensional “wavy” instability is the main mechanisms responsible for the emergence of the so-called *undulations patterns*.

As even a cursory comparative assessment of Figures 11 and 18 would immediately confirm, similar phenomena show up in the present circumstances when the lateral confinement is relaxed. Indeed, the latter figure clearly reveals a tendency of the present system to develop oblique rolls characterized by sinusoidal spatial distortions as the aspect ratio is increased from 10.6 to 17.7 and the straight (parallel) sidewalls are replaced by a curved boundary (although at this stage the role played in such a process by surface-tension effects in the present case is not clear).

As a concluding remark for this section, we wish to remark that these arguments should obviously be regarded for what they are, i.e., observations stemming from the quest for universality classes through the observation of companion or somehow related phenomena. Nevertheless, they point to interesting similarities in the underlying physics or mechanisms, which would require additional investigation in the frame of the linear stability analysis approach or other numerical techniques. Some general conclusions stemming from the present experimental work are elaborated accordingly in the next section.

6. Conclusions

Hybrid Marangoni-buoyancy convection in a fluid domain with variable fluid depth and inclined temperature gradient with respect to the horizontal direction has been investigated in the attempt to enrich the current knowledge about the fluid-dynamic behavior of these systems. In particular, the unique examined configuration should be regarded as an intentional attempt to move beyond the models adopted so far by the community of theoretical physicists and engineers, which has essentially been based on the paradigm of a series of different idealized setups and has not yet branched out to heated systems with irregular transversal thickness.

It has been shown that, in analogy with the companion cases represented by Marangoni convection in horizontal layers with temperature gradient inclined to the free liquid-gas interface and buoyancy convection in constant-thickness tilted enclosures, the preferred (or dominant) mode of convection for relatively small tilt angles is represented by longitudinal rolls. These manifest with a wavelength that increases with the layer depth. A relaxation in the lateral confinement can also contribute to increase their transverse extension, which indirectly proves that the sidewalls play role in the wavenumber selection mechanism in the considered range of aspect ratios.

A coherent picture of the richness of possible scenarios in terms of roll transverse size, longitudinal extension and orientation with respect to the tilt direction has been provided by varying parametrically the system influential factors, namely the temperature difference, liquid volume (average layer depth), inclination angle and the aspect ratio of the fluid container.

It has been shown that the hallmark of the considered dynamics is a modulation of the abovementioned transverse wavelength along the longitudinal direction, which should be regarded as an important distinguishing factor with respect to the “similar” behaviors displayed by these modes of convection in systems with a constant depth, regardless of whether the main driving force is represented by thermocapillarity or buoyancy. An increase in the temperature difference generally causes an increase in the longitudinal extension of the rolls.

Future attempts shall be devoted to clarify the nature of the interesting roll pinching mechanism (by which a single longitudinal roll can be split into two neighboring rolls with smaller wavelength), found in the case for which the lateral confinement is significant (small aspect ratio) and the layer depth is relatively small. Critical comparison with the existing literature has revealed that although most of existing results can be organized in well-studied universality classes, the interpretation of some experimental realizations

is not always a relatively simple task. Factors contributing to the inherent complexity of this objective are the essentially counter-intuitive non-linear behavior displayed by these systems and the blending of convective modes (normally operating separately) due to the nature of the specific problem considered here. Another open question relates to the influence of container shape. Although it has been proven here that the patterning behavior does not depend significantly on it (longitudinal rolls being selected over the entire space of parameters) and that the main impact of a variation in the aspect ratio is limited to a modification of the transverse roll extension, additional care shall be put to discern separately the role played by the container aspect ratio and its shape. The latter might indeed be the root cause of the differences observed in terms of monotonic or non-monotonic nature of the curves providing the relationship between the roll wavelength and the longitudinal coordinate.

Author Contributions: Conceptualization, M.L.; methodology W.W.; software, M.L.; formal analysis, M.L. and W.W.; investigation, W.W.; data curation, W.W. and M.L.; writing—original draft preparation, M.L.; writing—review and editing, M.L.; visualization, W.W.; supervision, M.L. All authors have read and agreed to the published version of the manuscript.

Funding: This research received no external funding.

Data Availability Statement: The data presented in this study are available on request from the corresponding author.

Conflicts of Interest: The author declares no conflict of interest.

References

1. Markham, B.L.; Rosenberger, F. Diffusive-convective vapor transport across horizontal and inclined rectangular enclosures. *J. Cryst. Growth* **1984**, *67*, 241–254. [[CrossRef](#)]
2. Bachran, A.; Reinshaus, P.; Seifert, W. Influence of Thermal Processing Parameters and Material Properties on Velocity Configurations in Semiconductor Melts during the Vertical Bridgman Growth Technique. *Cryst. Res. Technol.* **1998**, *33*, 27–36. [[CrossRef](#)]
3. Mizev, A.I.; Schwabe, D. Convective instabilities in liquid layers with free upper surface under the action of an inclined temperature gradient. *Phys Fluids* **2009**, *21*, 112102. [[CrossRef](#)]
4. Jones, A.D.W. Spoke patterns. *J. Cryst. Growth* **1983**, *63*, 70–76. [[CrossRef](#)]
5. Coriell, S.R.; McFadden, G.B.; Boisvert, R.F.; Sekerka, R.F. Effect of a forced Couette flow on coupled convective and morphological instabilities during unidirectional solidification. *J. Cryst. Growth* **1984**, *69*, 15–22. [[CrossRef](#)]
6. Webb, B.W.; Viskanta, R. Natural-convection-dominated melting heat transfer in an inclined rectangular enclosure. *Int. J. Heat Mass Transf.* **1986**, *29*, 183–192. [[CrossRef](#)]
7. Forth, S.A.; Wheeler, A.A. Coupled convective and morphological instability in a simple model of the solidification of a binary alloy, including a shear flow. *J. Fluid Mech.* **1992**, *236*, 61–94. [[CrossRef](#)]
8. Lappa, M. On the Formation and Propagation of Hydrothermal waves in Solidifying Liquid Layers. *Comput. Fluids* **2018**, *172*, 741–760. [[CrossRef](#)]
9. Salgado Sanchez, P.; Ezquerro, J.M.; Fernandez, J.; Rodriguez, J. Thermocapillary effects during the melting of phase-change materials in microgravity: Steady and oscillatory flow regimes. *J. Fluid Mech.* **2021**, *908*, A20. [[CrossRef](#)]
10. Salgado Sanchez, P.; Porter, J.; Ezquerro, J.M.; Tinao, I.; Laverón-Simavilla, A. Pattern selection for thermocapillary flow in rectangular containers in microgravity. *Phys. Rev. Fluids* **2022**, *7*, 053502. [[CrossRef](#)]
11. Lappa, M. *Thermal Convection: Patterns, Evolution and Stability*; John Wiley & Sons, Ltd.: Chichester, UK, 2009.
12. Zhang, J.; Sekimoto, A.; Okano, Y.; Dost, S. Numerical simulation of thermal-solutal Marangoni convection in a shallow rectangular cavity with mutually perpendicular temperature and concentration gradients. *Phys. Fluids* **2020**, *32*, 102108. [[CrossRef](#)]
13. Boura, A.; Gebhart, B. The stability of a vertical flow which arises from combined buoyancy modes. *AIChE* **1976**, *22*, 94–102. [[CrossRef](#)]
14. Qin, T.; Grigoriev, R.O. A numerical study of buoyancy-Marangoni convection of volatile binary fluids in confined geometries. *Int. J. Heat Mass Transf.* **2018**, *127*, 308–320. [[CrossRef](#)]
15. Lipps, F.B. Two-dimensional numerical experiments in thermal convection with vertical shear. *J. Atm. Sci.* **1971**, *28*, 3–19. [[CrossRef](#)]
16. Thorpe, S.A. Transitional phenomena and the development of turbulence in stratified fluids: A review. *J. Geophys. Res.* **1987**, *92*, 5231–5248. [[CrossRef](#)]

17. Farrow, D.E.; Patterson, J.C. On the stability of the near shore waters of a lake when subject to solar heating. *Int. J. Heat Mass Transf.* **1993**, *36*, 89–100. [[CrossRef](#)]
18. Richter, F.M. Convection and the large-scale circulation of the mantle. *J. Geophys. Res.* **1973**, *78*, 8735–8745. [[CrossRef](#)]
19. Weber, J.E. On the stability of thermally driven shear flow heated from below. *J. Fluid Mech.* **1978**, *87*, 65–84. [[CrossRef](#)]
20. Cliffe, K.A.; Winters, K.H. A numerical study of the cusp catastrophe for Bénard convection in tilted cavities. *J. Comput. Phys.* **1984**, *54*, 531–534. [[CrossRef](#)]
21. Mizushima, J.; Adachi, T. Structural Stability of the Pitchfork Bifurcation of Thermal Convection in a Rectangular Cavity. *J. Phys. Soc. Jpn.* **1995**, *64*, 4670–4683. [[CrossRef](#)]
22. Clever, R.M.; Busse, F.H. Instabilities of longitudinal convection rolls in an inclined layer. *J. Fluid Mech.* **1977**, *81*, 107–125. [[CrossRef](#)]
23. Chen, Y.; Pearlstein, A.J. Stability of free-convection flows of variable-viscosity fluids in vertical and inclined slots. *J. Fluid Mech.* **1989**, *198*, 513–541. [[CrossRef](#)]
24. Shadid, J.N.; Goldstein, R.J. Visualization of longitudinal convection roll instabilities in an inclined enclosure heated from below. *J. Fluid Mech.* **1990**, *215*, 61–84. [[CrossRef](#)]
25. Busse, F.H.; Clever, R.M. Three-dimensional convection in an inclined layer heated from below. *J. Eng. Math.* **1992**, *26*, 1–19. [[CrossRef](#)]
26. Fujimura, K.; Kelly, R.E. Mixed mode convection in an inclined slot. *J. Fluid Mech.* **1993**, *246*, 545–568. [[CrossRef](#)]
27. Kaloni, P.N.; Qiao, Z. On the nonlinear stability of thermally driven shear flow heated from below. *Phys. Fluids* **1996**, *8*, 639. [[CrossRef](#)]
28. Daniels, K.E.; Bodenschatz, E.; Pesch, W.; Brausch, O. Pattern formation in inclined layer convection; Session QC28—Topics in Pattern Formation and Nonlinear Dynamics. In Proceedings of the APS Centennial Meeting, Atlanta, GA, USA, 20–26 March 1999; Available online: <https://flux.aps.org/meetings/YR99/CENT99/abs/S6255001.html> (accessed on 20 November 2022).
29. Daniels, K.E.; Plapp, B.B.; Bodenschatz, E. Pattern Formation in Inclined Layer Convection. *Phys. Rev. Lett.* **2000**, *84*, 5320–5323. [[CrossRef](#)]
30. Daniels, K.E.; Brausch, O.; Pesch, W.; Bodenschatz, E. Competition and bistability of ordered undulations and undulation chaos in inclined layer convection. *J. Fluid Mech.* **2008**, *597*, 261–282. [[CrossRef](#)]
31. Tao, J.; Busse, F.H. Oblique roll instability in inclined buoyancy layers. *Eur. J. Mech. B/Fluids* **2009**, *28*, 532–540. [[CrossRef](#)]
32. Subramanian, P.; Brausch, O.; Daniels, K.E.; Bodenschatz, E.; Schneider, T.M.; Pesch, W. Spatio-temporal patterns in inclined layer convection. *J. Fluid Mech.* **2016**, *794*, 719–745. [[CrossRef](#)]
33. Nepomnyashchy, A.A.; Simanovskii, I.B.; Braverman, L.M. Stability of thermocapillary flows with inclined temperature gradient. *J. Fluid Mech.* **2001**, *442*, 141–155. [[CrossRef](#)]
34. Ueno, I.; Kurosawa, T.; Kawamura, H. Thermocapillary Convection in Thin Liquid Layer with Temperature Gradient Inclined to Free Surface. In Proceedings of the IHTC12, Grenoble, France, 18–23 August 2002.
35. Shklyaev, O.E.; Nepomnyashchy, A.A. Thermocapillary flows under an inclined temperature gradient. *J. Fluid Mech.* **2004**, *504*, 99–132. [[CrossRef](#)]
36. Patne, R.; Agnon, Y.; Oron, A. Thermocapillary instabilities in a liquid layer subjected to an oblique temperature gradient. *J. Fluid Mech.* **2021**, *906*, A12. [[CrossRef](#)]
37. Cerisier, P.; Pantaloni, J.; Finiels, G.; Amalric, R. Thermovision applied to Bénard-Marangoni convection. *Appl. Opt.* **1982**, *21*, 2153–2159. [[CrossRef](#)]
38. Cerisier, P.; Rahal, S.; Azuma, H. Pattern dynamics of the Bénard-Marangoni instability in a medium aspect ratio container. *J. Phys. Conf. Ser.* **2007**, *64*, 012004. [[CrossRef](#)]
39. Ismagilov, R.F.; Rosmarin, D.; Gracias, D.H.; Stroock, A.D.; Whitesides, G.M. Competition of intrinsic and topographically imposed patterns in Bénard–Marangoni convection. *Appl. Phys. Lett.* **2001**, *79*, 439–441. [[CrossRef](#)]
40. Chauvet, F.; Dehaeck, S.; Colinet, P. Threshold of Bénard-Marangoni instability in drying liquid films. *EPL Europhys. Lett.* **2012**, *99*, 34001. [[CrossRef](#)]
41. Wang, J.M.; Liu, G.H.; Fang, Y.L.; Li, W.K. Marangoni effect in nonequilibrium multiphase system of material processing. *Rev. Chem. Eng.* **2016**, *32*, 551–585. [[CrossRef](#)]
42. Wu, D.; Duan, L.; Kang, Q. Wavenumber Selection by Bénard–Marangoni Convection at High Supercritical Number. *Chin. Phys. Lett.* **2017**, *34*, 054702. [[CrossRef](#)]
43. Sobac, B.; Colinet, P.; Pauchard, L. Influence of Bénard–Marangoni instability on the morphology of drying colloidal films. *Soft Matter* **2019**, *15*, 2381–2390. [[CrossRef](#)]
44. Tönsmann, M.; Scharfer, P.; Schabel, W. Critical Solutal Marangoni Number Correlation for Short-Scale Convective Instabilities in Drying Poly(vinyl acetate)-Methanol Thin Films. *Polymers* **2021**, *13*, 2955. [[CrossRef](#)]
45. Gillon, P.; Homsy, G.M. Combined thermocapillary-buoyancy convection in a cavity: An experimental study. *Phys. Fluids* **1996**, *8*, 2953–2963. [[CrossRef](#)]
46. Braunsfurth, M.G.; Homsy, G.M. Combined thermocapillary-buoyancy convection in a cavity. Part II. An experimental study. *Phys. Fluids* **1997**, *9*, 1277–1286. [[CrossRef](#)]

47. Burguete, J.; Mukolobwicz, N.; Daviaud, N.; Garnier, N.; Chiffaudel, A. Buoyant-thermocapillary instabilities in extended liquid layers subjected to a horizontal temperature gradient. *Phys. Fluids* **2001**, *13*, 2773–2787. [[CrossRef](#)]
48. Pelacho, M.A.; Garcimartin, A.; Burguete, J. Travel instabilities in lateral heating. *Int. J. Bifurcat. Chaos* **2001**, *11*, 2881–2886. [[CrossRef](#)]

Disclaimer/Publisher’s Note: The statements, opinions and data contained in all publications are solely those of the individual author(s) and contributor(s) and not of MDPI and/or the editor(s). MDPI and/or the editor(s) disclaim responsibility for any injury to people or property resulting from any ideas, methods, instructions or products referred to in the content.